Europa's perturbed fields and induced dipole affect energetic proton depletions during distant Alfvén wing flybys

Huybrighs, H.L.F.; Blöcker, A.; Roussos, E.; Buchem, C.P.A. van; Futaana, Y.; Holmberg, M.K.G.; ... ; Witasse, O.

Citation

Note: To cite this publication please use the final published version (if applicable).

Correspondence to:

H. L. F. Huybrighs,
hans@cp.dias.ie

Europa's Perturbed Fields and Induced Dipole Affect Energetic Proton Depletions During Distant Alfvén Wing Flybys

H. L. F. Huybrighs[1,2,3,4] , **A. Blöcker[5,6]** , **E. Roussos[7]** , **C. van Buchem[1,8]** , **Y. Futaana[9]** , **M. K. G. Holmberg[1,4]** , **C. Goetz[1,10]** , **and O. Witasse[1]**

[1]European Space Agency (ESA), European Space Research and Technology Centre (ESTEC), Noordwijk, The Netherlands, [2]Space and Planetary Science Center, Khalifa University, Abu Dhabi, UAE, [3]Department of Mathematics, Khalifa University, Abu Dhabi, UAE, [4]School of Cosmic Physics, DIAS Dunsink Observatory, Dublin Institute for Advanced Studies, Dublin, Ireland, [5]KTH, Royal Institute of Technology, Stockholm, Sweden, [6]Department of Earth and Environmental Sciences, Ludwig Maximilian University of Munich, Munich, Germany, [7]Max Planck Institute for Solar System Research, Göttingen, Germany, [8]Leiden University, Leiden, The Netherlands, [9]IRF, Swedish Institute of Space Physics, Kiruna, Sweden, [10]Northumbria University, Newcastle-upon-Tyne, UK

Abstract We investigate the causes of energetic proton (80–540 keV) depletions measured during the two most distant flybys of Europa by Galileo, E17 and E25A, which encountered the Alfvén wings. First, by simulating the proton flux with a Monte Carlo particle tracing code we investigate the effect of: electromagnetic field perturbations, the induced dipole, atmospheric charge exchange and plumes. Inhomogeneous fields associated with the Alfvén wings and the ionosphere strongly affect the depletions. For homogeneous fields the depletion along the trajectory is focused on a narrow pitch angle range and has no structure, whereas the depletion for perturbed (inhomogeneous) fields represents a wider and complex structure. Furthermore, also the induced dipole alters the depletion structure. The effect of plumes (density 2.5×10^{15} m^{-3}) and charge exchange on the proton depletion is minor. Second, we compare the simulations to the proton measurements. The simulations with inhomogeneous fields describe the data qualitatively better than the homogeneous case, suggesting that indeed field perturbations are responsible for the measured losses. We attribute discrepancies between the simulations and the proton measurements to discrepancies between the simulated and real fields. We argue that simulating the fields along the trajectory is a good first step, but that ideally the energetic ion flux is reconstructed well to gain confidence in the interpretation of the simulated magnetic field. In conclusion, energetic ion observations along distant flybys through the Alfvén wings are suitable for isolating the characteristics of the global configuration of the magnetospheric interaction region of Europa (or other moons).

Plain Language Summary Europa is a moon of Jupiter with a potentially habitable subsurface ocean. Located in Jupiter's giant magnetic field, it is exposed to extremely fast protons. Galileo measured the disappearance of normally abundant protons when it encountered Europa's Alfvén wings, during its two furthest flybys. The Alfvén wings are cylindrical regions of disturbed magnetic field, extending north and south of Europa. Using simulations of the protons' motion we show that disturbances of the magnetic field associated with the Alfvén wings and Europa's ionosphere can deflect fast protons and cause their local disappearance. Europa's ocean, which causes an induced magnetic field of its own, will also modify the proton losses. Europa's ocean thus influences the motion of protons at distances of several 1,000 km. This effect could be used by future missions to find evidence of oceans on other moons, such as Triton. Lastly, the simulations with disturbed magnetic fields have a better qualitative agreement with the measurement, as opposed to those without. This implies that the field perturbations are indeed affecting the proton disappearances. We argue that to gain confidence in our understanding of the magnetic field, both the magnetic field measurements and the energetic ion measurements should be reproduced well.

1. Introduction

Europa, the fourth largest moon of Jupiter (radius 1,569 km), is thought to harbor a potentially habitable water ocean under its surface. It resides in Jupiter's inner magnetosphere at a distance of 9.38 Jupiter radii (1 R_J = 71,492 km) from Jupiter's center. Europa is exposed to two populations of charged particles: relatively low energy co-rotating plasma and highly energetic charged particles (Kivelson et al., 2009). Europa, its atmosphere,

Table 1
Orbits of Interest for This Paper

Flyby	Date	Day of the year	C.A. time [U.T.]	C.A. altitude [km]
E17	26 Sept 1998	269	03:54:20	3587.4
E25A	25 Nov 1999	329	16:29:05	8,580

Note. C.A. refers to closest approach.

and its erupting water plumes affect the local magnetospheric environment. Of particular relevance for this work are depletions of the energetic proton flux that were measured by the Energetic Particle detector EPD on Galileo (Williams et al., 1992) during the E17 (closest approach 3,587 km) and E25A (closest approach 8,580 km) flybys of Europa, the most distant flybys of Europa by Galileo. With E25A we refer to the segment of Galileo orbit I25, during which the spacecraft passed close by Europa. Details for the flybys are provided in Table 1. The depletions coincide with the encounter of Europa's Alfvén wings, the latter were demonstrated using magnetic field measurements by Volwerk et al. (2007). The Alfvén wings are two cylindrical regions of disturbed magnetic field and plasma flow extending both north and south of Europa (Kivelson et al., 2009; Neubauer, 1980).

Our goal is to investigate the nature of these energetic proton depletions that occur at several Europa radii. We emphasize that the particle data is also an important data set to constrain the magnetic field configuration near Europa. As will be discussed in the next paragraphs, the depletions of the energetic protons are affected by the perturbed electromagnetic fields. While field measurements only provide measurements along the field, particles sample the field relatively globally. Furthermore, the approach being tested here is also valuable for studying moon-magnetosphere interaction at data starved targets other than Europa. Possible applications may be flybys of Ice Giant moons, for example, at Triton.

In the next paragraphs we review different effects that have been proposed as playing a roll in the loss of energetic ions near Europa and other moons, for Europa specifically: impact of the energetic ions on the surface (e.g., Paranicas et al., 2000; Paranicas et al., 2007, 2008), deflection of the protons by inhomogeneous electromagnetic fields (e.g., Addison et al., 2021, 2022; Breer et al., 2019; Nordheim et al., 2022; Paranicas et al., 2000), charge exchange of the protons with atmospheric neutrals and the effect of potential plumes on the protons through deflection by perturbed fields and charge exchange (Huybrighs et al., 2020). Note that we refer to any kind of flux dropout as "depletion," be it due to surface impact, charge exchange or Galileo encountering a "forbidden region" from which protons are deflected (e.g., Paranicas et al., 2000; Roussos et al., 2012).

Energetic ions that impact the surface are absorbed and therefore result in a depletion. Such type of depletions have been widely reported at various moons of Saturn, such as Dione, Janus, Mimas and Rhea (e.g., Kotova et al., 2015; Krupp et al., 2020; Paranicas et al., 2008), and moons of Jupiter such as Amalthea, Thebe and the Galilean moons (e.g., Kivelson et al., 2004; Roussos et al., 2022). Specifically for Europa Paranicas et al. (2000, 2007) attributed measured energetic ion depletions during flybys E12 and E26, respectively, to absorption by Europa's surface.

Furthermore, a magnetic field gradient can restrict access of energetic charged particles in a certain region, creating a "forbidden region," as suggested by for example, Paranicas et al. (2000) for Europa and by Roussos et al. (2012) for energetic electrons at Saturn's moon Rhea. Near Europa perturbations in the electromagnetic field are caused by the interaction of the magnetospheric plasma with Europa's tenuous atmosphere and ionosphere, water plumes and by the signal from a subsurface water ocean due to Jupiter's time-varying magnetic field in Europa's reference frame (Arnold et al., 2019; Jia et al., 2018; Schilling et al., 2007). Paranicas et al. (2000) attributes ion depletions during flyby E12 to drift motions resulting from gradients in the inhomogeneous magnetic field (in addition to surface impact). Furthermore, studies such as Breer et al. (2019), Addison et al. (2021, 2022) and Nordheim et al. (2022) have shown that the precipitation pattern of energetic ions on the surface of Europa is affected by inhomogeneous (perturbed) fields resulting from the induced dipole and plasma interaction with Europa's atmosphere and plumes.

Charge exchange with atmospheric neutrals causes energetic protons to turn into energetic neutral atoms (ENA) resulting in the depletion of energetic protons. Atmospheric charge exchange has been investigated as a loss process of energetic ions at Saturn's moons Titan (e.g., Mitchell et al., 2005; Wulms et al., 2010), and also Rhea where the effect has been found to be not significant (Kotova et al., 2015). Lagg et al. (2003) and Kollmann et al. (2016) reported losses of protons (80–220 keV) by charge exchange with Europa's neutral torus. Addison et al. (2021) showed that the total surface flux of energetic protons (below 100 keV) is reduced by a factor of 2–3 due to charge exchange with atmospheric neutrals, with the greatest reduction occurring near the trailing hemisphere apex. Furthermore, water vapor plumes provide an additional source of

neutrals. Their existence has been suggested by multiple studies (Arnold et al., 2019; Blöcker et al., 2016; De La Fuente Marcos & Nissar, 2000; Jia et al., 2018; McGrath & Sparks, 2017; Paganini et al., 2019; Roth et al., 2014; Sparks et al., 2016, 2017, 2019). The increased neutral density in the plume enhances charge exchange and causes local perturbations of the electromagnetic fields in the near environment and in the Alfvénic far field of Europa. The effect of these field perturbations on proton depletions has not been investigated.

Huybrighs et al. (2020) demonstrated, using a Monte Carlo particle tracing code, that proton depletions (115–244 keV) during Galileo flyby E26 were affected, in addition to surface impact, by atmospheric charge exchange and inhomogeneous fields. Furthermore, Huybrighs et al. (2020) showed that plumes could, in principle, cause proton depletions through charge exchange and field perturbations. A single proton depletion feature identified as a potential plume signature was later shown to be affected by an artifact, preventing a definitive conclusion on the presence of a plume (Huybrighs et al., 2021; Jia et al., 2021).

Nénon et al. (2018) proposes that near Io ion cyclotron waves could resonate with energetic protons and cause proton losses. Shprits et al. (2018) reports the existence of whistler waves near Europa and suggest that they could cause depletions in phase space density. However, we do not consider that the depletion due to wave particle interaction is likely a major contributor in this situation. First, our previous work Huybrighs et al. (2020, 2021) demonstrates that we can explain the fine structure of the energetic proton losses at Europa (100 keV–1 MeV), with a combination of impact on the surface, charge exchange and perturbed fields, thus there is no need to invoke wave particle interactions. Second, the proton depletion features that we are interested in are confined to the Alfvén wing encounter, which is not a region of enhanced ion production and therefore not expected to have more pronounced ion cyclotron waves than the surrounding regions (where no losses occur).

In this work we investigate the cause of the depletions during the E17 and E25A flybys, which are known to have encountered the Alfvén wings based on magnetic field measurements (Volwerk et al., 2007). Europa's Alfvén wings are formed when the corotating plasma is slowed down in front of Europa. The slowing down of the plasma occurs because of the interaction between the magnetospheric ions and the atmospheric neutrals via elastic collisions, charge exchange and ionization. The generated plasma flow and magnetic field perturbations propagate north and south of Europa in the form of standing Alfvén waves. The relative difference in speed between the slowed-down plasma in front of Europa and the undisturbed regions results in a bending of the mainly southward pointing magnetic field lines in the direction of the flow, which is toward the trailing side of Europa. The plasma flow is directed around the Alfvén wings and its velocity is strongly decreased inside the Alfvén wings. Neubauer (1999) demonstrated that the induced dipole related to the ocean affects the Alfvén wings resulting in a shrinkage and displacement of the wings. Furthermore, Blöcker et al. (2016) have demonstrated that atmospheric inhomogeneities near the North and South pole cause north-south asymmetries of the electromagnetic fields in the Alfvén wings in the form of Alfvén winglets. Harris et al. (2021) have shown that the angle of the Alfvén wings with respect to the ambient magnetic field increases with increasing ambient plasma density. At other moons it has been demonstrated that Alfvén wings and draped fields affect the motion of energetic ions, for example, at Titan energetic protons are deflected away from the moon by draped fields (Wulms et al., 2010), while at Ganymede the circulation of energetic ions near Ganymede's polar caps is strongly determined by the Alfvén wings (Plainaki et al., 2020). At Callisto Liuzzo et al. (2019b) has established that energetic protons can be deflected by the Alfvén wings. At Io, Selesnick and Cohen (2009) have demonstrated, using ion backtracing simulations, that losses of energetic oxygen and sulfur ions (>5 MeV/nucleon) measured by Galileo's Heavy Ion Counter (HIC) during Io flybys I27, I31 and I32 could be attributed to surface impact and the effect of field perturbations due to Io's Alfvén wings. Selesnick and Cohen (2009) accounted for the Alfvén wing perturbations using a highly idealized analytical description of the magnetic field associated with the wings. The addition of the Alfvén wings provides for a better reproduction of the measured ion dropouts during polar flybys I31 and I32. The Alfvén wings at certain segments of the flyby acting to deflect ions that would otherwise collide with Io's surface, while enhancing losses in other segments. For non-polar flyby I27 the effect of the Alfvén wing is small.

At Europa it has not been investigated whether different Alfvén wing configurations have a sufficiently diverse impact on the energetic ion distributions so that they can be used for investigations of a deeper understanding of Europa's interior and external environment in particular so during distant flybys. Second, the EPD data collected during E17 and E25A offer a unique opportunity to investigate the validity of the energetic proton and electromagnetic field models.

In this study we investigate the formation of the proton losses by simulating the flux of energetic protons using a Monte Carlo particle backtracing method. The first key aspect of this paper concerns a modeling exercise in which we investigate the effect of the Alfvén wings, ionospheric field perturbations, the induced dipole and plumes on the energetic proton losses during distant flybys. By ionospheric perturbations we refer to field perturbations caused by the plasma interaction with Europa's atmosphere, they are strongest close to the moon and their influence on the fields is also visible a few moon radii away from the moon. The second key aspect concerns the comparison of the simulated proton flux with the Galileo EPD measurements.

Particle tracing studies have been conducted at various moons, for example, at Jupiter's moons Europa (Addison et al., 2021; Breer et al., 2019; Cassidy et al., 2013; Nordheim et al., 2022), Ganymede (Carnielli et al., 2019, 2020a, 2020b) and Callisto (Liuzzo et al., 2019a, 2019b, 2022), at Saturn's moon Titan (Modolo & Chanteur, 2008; Regoli et al., 2016; Snowden et al., 2018; Snowden & Higgins, 2021; Tippens et al., 2022), at Earth's moon using backtracing (Futaana et al., 2003) or at Mars and Phobos (Curry et al., 2014; Futaana et al., 2010). Ion depletions have been investigated using particle tracing, for example, at the Jovian moon Io and Ganymede (Poppe et al., 2018; Selesnick & Cohen, 2009) and Saturnian moons Dione, Rhea and Titan (Kotova et al., 2015; Wulms et al., 2010).

Considering that previous studies have established that surface impact, inhomogeneous fields and atmospheric charge exchange can affect the proton depletions, we will consider each of these effects. Because of the large distance of these flybys, around 3,587 km or 2.3 Europa radii (R_E) for E17 and 8,580 km or 5.5 R_E for E25A, we expect the main perturbation to be the one associated with the Alfvén wings because of their translational invariance along the field lines. We will also investigate the effect of plumes and the induced dipole, which can affect the Alfvén wings by, respectively, introducing winglets inside the main Alfvén wing-tubes, and displacing Alfvén the wings as well as shrinking the wing tube cross sections (Neubauer, 1999; Volwerk et al., 2007).

2. E17 and E25A Measured Proton Depletions

During both flybys, E17 and E25A, energetic proton depletions (80–540 keV) were observed during or near the Alfvén wing encounter. For both flybys, only data from two EPD proton channels are available: TP1 (80–220 keV) and TP2 (220–540 keV). Furthermore only a low resolution data product is available. This data product is referred to as "LGA," which refers to the Low Gain Antenna it was transmitted through.

An overview of the data and flyby geometry is shown in Figure 1. The Cartesian coordinate system used in this work is the EPhiO system with its x axis along the direction of the magnetospheric plasma flow, the z axis is parallel to Jupiter's spin axis, and the y axis is facing Jupiter.

Channels TP1 and TP2 are part of the Composition Measurement System (CMS) of the EPD telescope (Williams et al., 1992). CMS uses a time of flight mass spectrometer to separate protons from other ions and a triple coincidence detection system to limit the effect of noise by penetrating radiation. The EPD telescope can scan the whole sky in ~140 s using the combined motion of a rotating platform that moves through 7 motor positions and the ~20 s period spacecraft spin (Williams et al., 1992). The EPD CMS channels have an opening angle of 18°. Note that no data is available for the TP3 channel (540–1,040 keV) for both E17 and E25A.

The EPD proton channel TP1 (80–220 keV) is particularly suitable for finding signatures of atmospheric charge exchange because the cross section for charge exchange between H^+ and O_2 at the energies covered by TP1 is the largest compared to the other (higher) energy proton channels (see Figure A1). The cross section in TP2 is orders of magnitude lower and therefore TP2 is significantly less sensitive to atmospheric charge exchange. Moreover, for the proton channels less free parameters are involved compared to other measured ion species (e.g., oxygen or sulfur), as the protons have a known charge state, while oxygen and sulfur could have higher charge states (Clark et al., 2016; Nénon & André, 2019). Additionally there are large uncertainties in the charge exchange cross section for those species. Finally, the energies involved are small enough for gyration scales (see Figure B1) to be sensitive to inhomogeneous fields.

The proton depletions can be seen in Figure 1 as the darkest points of the colorbar during the Alfvén wing encounters, of which the entry and exit points are indicated by the black dashes (as discussed in Appendix D). The EPD data has been exported using the software from previous EPD studies, for example, Lagg et al. (2003). The left column of the Figure shows the data of the TP1 channel (80–220 keV), while the right panel shows the
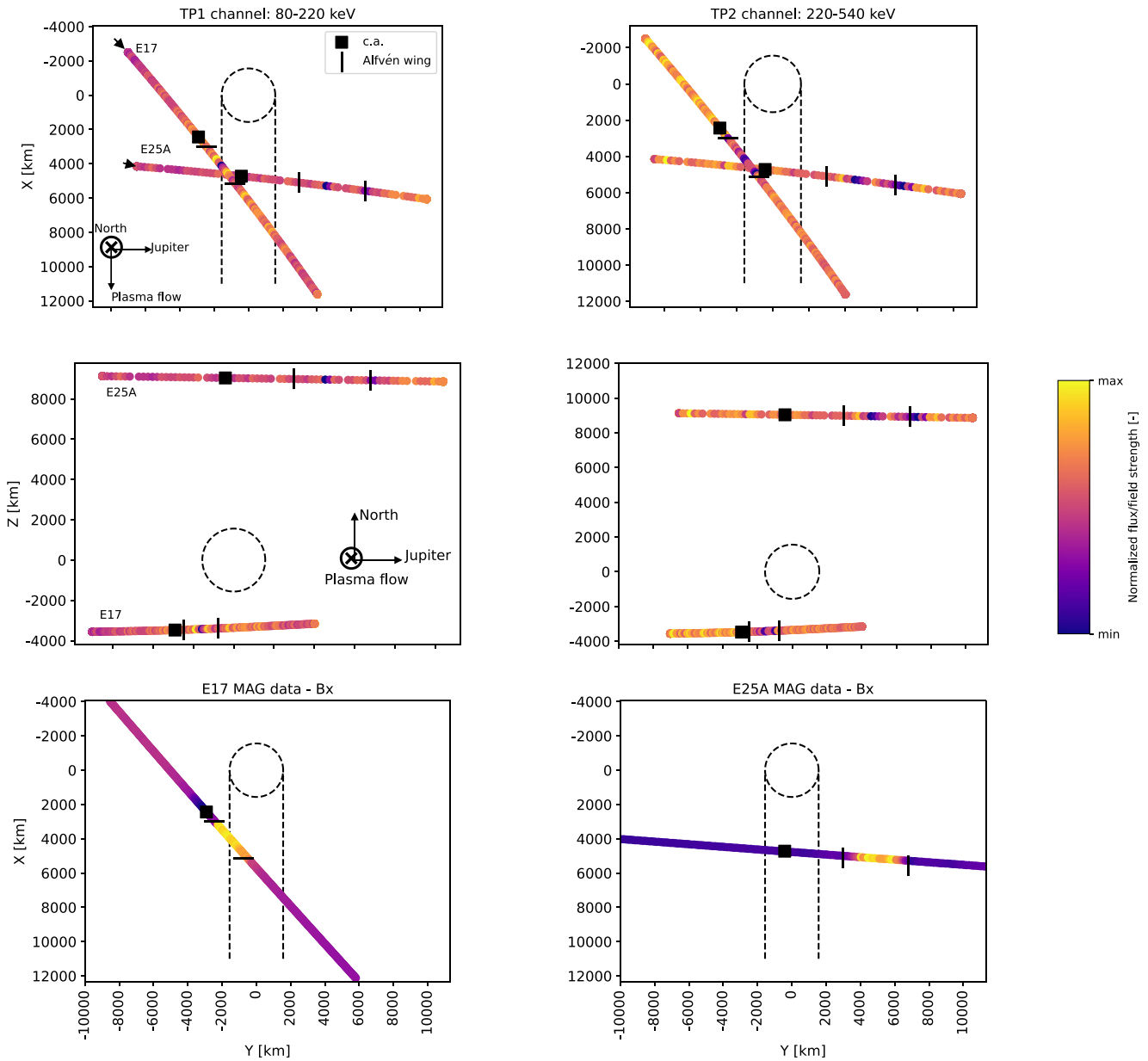
Figure 1. Measured proton flux during flybys E17 and E25A (row 1–2) and the measured Bx component of the magnetic field (bottom row left for E17 and right for E25A). Note in particular the depletions near or between the Alfvén wing encounters marked by the black dashes along the trajectory. The left panels (row 1–2) show the 80–220 keV energy channel (TP1) and the right panels (row 1–2) the 220–540 kev channel (TP2) in the xy plane and yz plane. Note that the EPD data is provided in blocks of 16 datapoints spanning 228 (E17) or 342 (E25A) seconds. Within each block an uncertainty in the time of each measurement exists of maximum 228 s (E17) or 342 s (E25A), or about 5% (E17) or 7% (E25A) of the length of the plotted trajectories. Furthermore, within every block of 16 datapoints the order of the measurements is arbitrary. Therefore, this figure can only be used to infer the approximate location of the depletion features within the uncertainties of 228–342 s (more details in the body of the text and Appendix E). For each flyby the proton and magnetic field data are normalized, respectively, to the mean proton flux and mean Bx value of the flyby. The black square indicates the closest approach. The dashed circle indicates Europa. Dashed lines show the direction of Europa's geometrical wake.

data for the TP2 channel (220–540 keV). The data have been normalized to the mean of each flyby. The bottom panels of Figure 1 also show the measured Bx component of the magnetic field. In the Bx component the effect of the Alfvén wing is most pronounced. Line plots of magnetic field data are also shown in Figure 12. The E17 flyby encounters the southern wing, while E25A encounters the northern wing. Depletions are visible in the Alfvén wing encounters during both flybys and in both energy channels. We consider that these depletions are aspects of the interaction with the Alfvén wings, and not a disturbance from the magnetosphere, as these depletions are
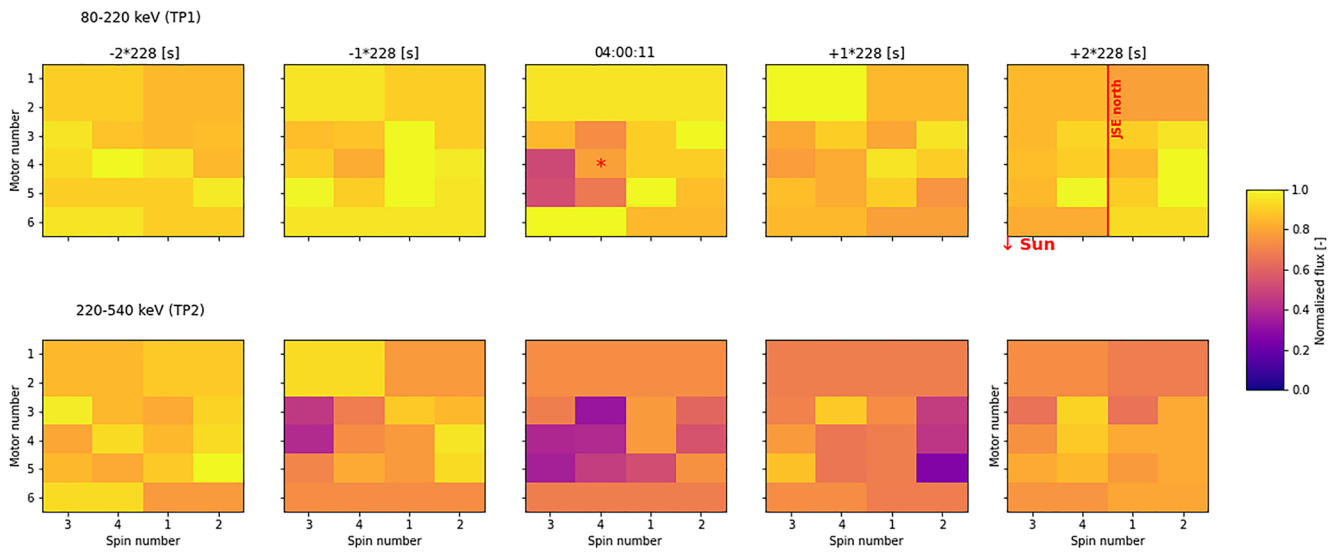
Figure 2. Measured proton flux during flyby E17 represented by skymaps. The top row represents the 80–220 keV channel (TP1) and the bottom row represents the 220–540 keV channel (TP2). This figure visualizes in which part of the sky (sector) the depletion occurred. Darker colors represent the depletions. Each skymap is composed of 16 sectors that have been averaged during two instrument cycles (or equivalently two unaveraged skymaps) lasting 228 s in total. For the measurements in each sector there is a maximum uncertainty of 228 s about when it occurred. The starting time of the middle panel is indicated above the panel. The red star in the middle panel indicates the sector closest to Europa, during the composition of the first of the two skymaps that have been averaged onboard the spacecraft to obtain the middle panel. The starting time of the other panels are expressed relative to the middle one. EPD skymaps are provided in the JSE frame (Jovicentric Solar Ecliptic), JSE north and the direction of sun are indicated in the top right panel. The horizontal axis represents the spin axis, where the spin number indicates the order of measurement. The vertical axis represents the axis scanned by moving the EPD motor over positions 1 to 6. A detailed description about how skymap is composed can be found in Appendix E.

only observed during or in the immediate vicinity of the Alfvén wing encounters as established from the magnetic field data.

Note that for flybys E17 and E25A only a low resolution data product (LGA) is available, which as a main limitation has an inherent uncertainty of maximum 228 s (E17) or 342 s (E25A) when an observation was made. Therefore, the exact location along the trajectory of the measured depletions is not known. However, since 228 or 342 s corresponds to approximately 5% and 7% of the duration of the plotted trajectories, it is clear that the proton depletions along both trajectories only occur during, or in the immediate vicinity of the Alfvén wing encounters. Therefore we consider that these dropouts are a feature that is related to the Alfvén wings, despite the uncertainty in the data.

The 228 (E17) or 342 (E25A) second uncertainty follows from the way measurements were stored in the LGA mode: they are stored in skymaps of 16 sectors that together represent the sky and were accumulated over two (E17) or three (E25A) instrument cycles. During each cycle the sky is scanned once, or equivalently, one skymap is generated. Thus, by combining different cycles, effectively two or three skymaps are averaged. The initial non-averaged skymaps are not transmitted to Earth, only the averaged skymaps. Therefore, it cannot be determined if a measurement was obtained during the first, second or third cycle, thus resulting in a maximum uncertainty of 228 s (E17) or 342 s (E25A) of the time of the measurement. The order in which the 16 values are stored in the PDS archive does not represent the order in which the measurement has been taken, but rather the sector of the sky it corresponds to, as opposed to the high resolution mode (which is referred to with the acronym HGA, from High Gain Antenna) wherein data are stored in the sequence they are measured in. For Figure 1 the data points are plotted in the order that they were stored in, meaning that within every block of 16 datapoints (or sectors) representing 228 (E17) or 342 (E25A) seconds of measurements, we do not know exactly when the measurement occurred. Therefore we emphasize that this figure can only be used to infer the approximate location of the depletion features within the uncertainties of 228–342 s. Further technical details about the LGA data product are provided in Appendix E.

In Figures 2 and 3 the LGA data is represented in the 16 sector sky maps that they were stored in after the averaging process described above. The skymaps reveal in which part of the sky (sector) the depletions occurred,
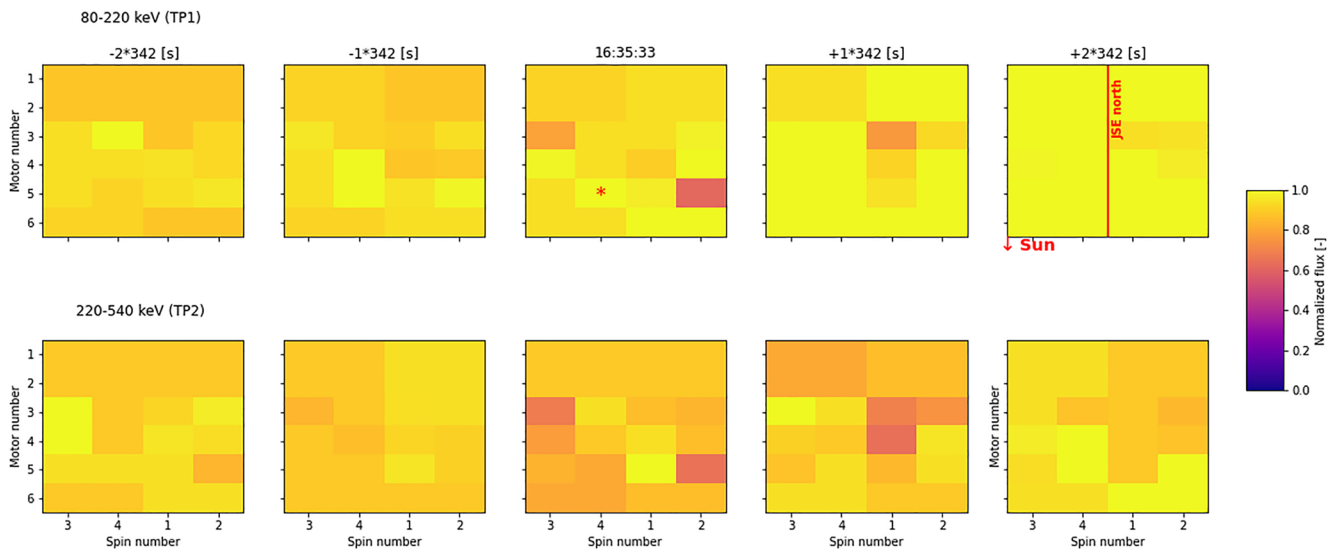
Figure 3. Measured proton flux during flyby E25A represented by skymaps. The top row represents the 80–220 keV channel (TP1) and the bottom row represents the 220–540 keV channel (TP2). This figure visualizes in which part of the sky (sector) the depletion occurred. Darker colors represent the depletions. Each skymap is composed of 16 sectors that have been averaged during three instrument cycles (or equivalently three unaveraged skymaps) lasting 342 s in total. For the measurements in each sector there is a maximum uncertainty of 342 s about when it occurred. The starting time of the middle panel is indicated above the panel. The starting time of the other panels are expressed relative to the middle one. The red star in the middle panel indicates the sector closest to Europa, during the composition of the first of the three skymaps that have been averaged onboard the spacecraft to obtain the middle panel. EPD skymaps are provided in the JSE frame (Jovicentric Solar Ecliptic), JSE north and the direction of sun are indicated in the top right panel. The horizontal axis represents the spin axis, where the spin number indicates the order of measurement. The vertical axis represents the axis scanned by moving the EPD motor over positions 1 to 6. A detailed description about how skymap is composed can be found in Appendix E.

because the information about the location of a measurement on the sky is preserved during the averaging process described above. Due to the averaging process, we only know in which sector a depletion occurred, but not exactly when, with a maximum uncertainty of 228 (E17) or 342 (E25A) seconds. The results of our particle tracing simulations will be represented in the same sky maps to allow for a comparison. Note that almost the full sky is scanned, as the EPD motor positions from 1 to 6 are scanned during this mode. Motor position 7, which has shown to be affected by an artifact that creates nonphysical dropouts (Huybrighs et al., 2021; Jia et al., 2021), is the only position not included in this mode.

We observe that localized proton depletions occur in different sectors of the sky maps. The depletions are thus not homogeneously spread over the sky. We also observe that the sectors where depletions occur in the lower energy channel (80–220 keV), correspond to sectors in higher energy channel (220–540 keV) that are also depleted.

We do not attribute the measured depletions to charge exchange with Europa's neutral torus because such torus-depletions are co-located with Europa's orbit and are not a localized feature (Kollmann et al., 2016; Lagg et al., 2003; Nénon & André, 2019). Furthermore, if the depletions were primarily driven by charge exchange we would expect the depletion in the TP2 channel to be less pronounced than in the TP1 channel, due to the decrease in the charge exchange cross section. This is not what we observe in the measurements.

3. Simulation Cases

Next we provide an overview of the different simulation cases that we consider for the particle tracing. We consider cases with homogeneous fields (no Alfvén wing or ionospheric perturbations) and compare them with inhomogeneous fields (with Alfvén wing and ionospheric perturbations). Despite that the situation with homogeneous fields is not expected to occur at Europa in reality, we consider this comparison relevant to determine the effect of the inhomogeneous fields, in particular the occurrence of the Alfvén wings and ionospheric perturbations on the proton depletions, as well as demonstrate that this difference is measurable. In addition we also consider cases that include atmospheric charge exchange and a plume. An induced dipole from the subsurface

Table 2
Parameter Values Used in the Particle Tracing Simulations

Parameters particle tracing simulation	Value
Integration time step particle trajectory [s]	0.0005
Number of integration time steps per gyration	300
Maximum number of time steps per particle	400,000
Number of particles per spacecraft trajectory step	10,000
Number of energy bins	10
Number of pitch angle bins	64
Spacecraft trajectory time step [s]	20

ocean is always included in the inhomogeneous cases, unless specifically mentioned. No dipole is included in the homogeneous cases.

To investigate the effect of the Alfvén wings and ionospheric perturbations on the proton depletions we consider the following simulation cases for each of the two flybys:

- Case 1: homogeneous electromagnetic fields, no atmospheric charge exchange
- Case 2: homogeneous electromagnetic fields, atmospheric charge exchange
- Case 3: inhomogeneous electromagnetic fields, no atmospheric charge exchange
- Case 4: inhomogeneous electromagnetic fields, atmospheric charge exchange

For flyby E17 we consider the following additional cases:

- Case 5: a plume at the south pole, inhomogeneous electromagnetic fields, atmospheric charge exchange.
- Case 6: induced dipole turned off, inhomogeneous electromagnetic fields, atmospheric charge exchange.

During the E17 flyby, Galileo was located in the high plasma density region near the plasma sheet center and passed through the southern Alfvén wing. A plume at the south pole would create a southern Alfvén winglet and would strongly affect the structure of the southern Alfvén wing according to Blöcker et al. (2016). The effect of a polar plume on the fields in the Alfvén wings is larger than a equatorially located plume. In order to investigate whether signatures of a plume in the atmosphere are present in the EPD data we include a plume which is located at the south pole. Most of the putative plume sources are indeed located on Europa's southern hemisphere (Winterhalder & Huybrighs, 2022).

Case 6, in which the dipole is turned off, is introduced as a theoretical exercise to investigate the effect of the induced dipole on the energetic proton depletion. A similar approach was used previously in Breer et al. (2019) and Nordheim et al. (2022). Physically, the case without induced dipole would resemble the situation the most when Europa is in the current sheet (low magnetic latitude), this is when the induction signal is the weakest. The induction signal is highest when furthest away from the current sheet center (higher magnetic latitude) (Neubauer, 1999). for E25A the magnetic latitude is 9.9° and for E17 it is 3.6° (Volwerk et al., 2007), so neither are at the magnetic equator. Induced dipole parameters are the same as those in Section 2.1.4 in Blöcker et al. (2016). For the ocean we assume a conductance of 0.5 S/m, based on Schilling et al. (2007) which is the same value as used by Blöcker et al. (2016).

For flyby E25A we consider the following additional cases:

- Case 7: a plume located at the North pole, inhomogeneous electromagnetic fields and atmospheric charge exchange.
- Case 8: induced dipole turned off, inhomogeneous electromagnetic fields and atmospheric charge exchange.

During E25A, Galileo passed downstream through the northern Alfvén wing. In this case we put the plume on the north pole to see what effect the northern Alfvén winglet would have on the EPD data measured during this flyby. While no potential plume has been explicitly located on the northern hemisphere, the potential plume from Paganini et al. (2019) does not have a latitudinal constraint. It could thus have occurred on the northern hemisphere. Furthermore, due to an overall limited number of observations it cannot be excluded that plumes are also located on the northern hemisphere, therefore we also consider such a hypothetical case.

4. Method: Particle Tracing

We simulate the measured flux of energetic protons using a Monte Carlo particle backtracing code, developed from Huybrighs et al. (2017, 2020). The input parameters are summarized in Table 2. We treat energetic protons as test particles because they have no influence on the electromagnetic fields, as their number density is small compared to that of the low energy plasma. Each proton is traced back in time from the EPD detector and it is determined if it impacts and/or charge exchanges. By performing this analysis for many particles the depletion is

determined as a fraction of the (normalized) undisturbed flux. The different steps of this process, from particle launch to impact are elaborated on in the next paragraphs.

We consider two types of simulations. For the first type the flux of protons for every position along the spacecraft trajectory and at every pitch angle (0–180°) is evaluated. 20 second time steps are considered for the spacecraft trajectory. The results of these simulations provide a global view of the depletion of energetic protons occurring along the spacecraft trajectory, thereby providing us with an idea of what an ideal instrument with a high temporal and spatial resolution could measure. In the second type the EPD pointing as well as the data sectoring and averaging are reproduced to simulate the measured flux. The results of these simulations allow a closer comparison with the data.

For the first type of simulation, particles are launched at a pitch angle according to a uniform distribution using the Monte Carlo method, within the range 0–180°. For the second type of simulations particles are traced back from the EPD detector, thereby taking into account the pointing of the instrument and the location of the Galileo spacecraft. Appendix E describes how we estimated the pointing of EPD. An 18° opening cone is assumed for the EPD instrument. Using the Monte Carlo method particles are launched at a random angle within the opening cone following a uniform distribution. The exact point of origin of the particle is assumed to be the location of the spacecraft.

The distribution of the proton flux with energy is taken into account in the simulation. Using the Monte Carlo method, particles are launched at a random energy within the energy range of the TP1 channel. After generation the particles are binned according to energy (10 bins) and pitch angle (64 bins) at launch. The energetic proton flux decreases with increasing energy. Therefore, for each energy channel, TP1 or TP2, the flux is higher at the lower energy end than at the higher energy end. To account for this decrease in flux over the energy range of the channels we weight the particles according to the energy distribution of the flux. This is achieved by binning the particles in ten logarithmically spaced energy bins and applying a weighting according to a pre-selected energy spectrum. For this study we used the spectrum from Huybrighs et al. (2020), in this previous study we found that using the spectra from other flybys had no significant impact on the result.

Trajectories of protons are traced back in time by numerically integrating the Lorentz force using a leap frog integration scheme (Huybrighs et al., 2017, 2020). The backtracing method results in a reduction of computing resources compared to forward tracing, as only the trajectories of particles that could enter the detector are simulated. Parameter settings for the particle tracing are summarized in Table 2. The timestep size of 5×10^{-4} s was determined by running simulations with decreasing timestep size. The time step needs to be sufficiently small to resolve the gyroradius of the particles. We found that decreasing the timestep further had no significant effect on the simulated depletions.

To simulate the trajectories of energetic ions a description of the electromagnetic field is required. We consider both a homogeneous field and an inhomogeneous field (the latter is discussed in the next section). For the homogeneous case any perturbations in the field arising due to the interaction of the corotational plasma with Europa are neglected, as well as the contribution of Europa's induced dipole. The homogeneous magnetic field **B** is obtained from the Galileo MAG data. We interpolate the magnetic field data before and after the moon encounter, to account for the trend of the background magnetic field during the flyby. From this interpolation we use the value at the closest approach to obtain **B**. The electric field **E** is calculated from **B** using the relation $\mathbf{E} = -\mathbf{v} \times \mathbf{B}$, in which **v** is the velocity of the corotational plasma. The values for **B** and **v** in the homogeneous cases are the same as the initial values used for the MHD simulations (see Table 4).

Ions are traced until 8 R_E for E17 and until 9 R_E for E25A and then removed from the simulation. The furthest distance was chosen to be ∼1 R_E larger than the furthest removed spacecraft trajectory point from which particle tracing is performed. As will be shown the next sections the predicted depletions are concentrated close to the Alfvén wing encounter, disappearing well before the furthest spacecraft trajectories points. We thus consider the margin of ∼1 R_E as sufficient. Since the bounce periods of the protons are around several hundred seconds (see Figure C1), they will not encounter Europa again when the fields are homogeneous. However, as will be shown later in the case of the inhomogeneous/perturbed fields some of the backtraced protons, downstream of Europa will instead locally mirror between the Alfvén wings and impact Europa.

Unlike our earlier work (Huybrighs et al., 2020, 2021) we neglect the pitch angle distribution of the protons. For these particular flybys the resolution at which the proton data is provided is not sufficient to determine the pitch

angle distribution. Effectively we assume a uniform pitch angle distribution. Because of this simplification, our simulations will not reproduce the background pitch angle distribution. However, we consider that this a viable approach because our simulations will show the deviation from the background distribution near the Alfvén wing encounter, specifically proton losses localized to the wing encounter. The proton losses near the Alfvén wing encounter are much more pronounced features than any variations in the upstream distribution. This can be concluded by comparing the middle panel in Figures 2 and 3 with the last and final panels of the respective figures, which are representative for the undisturbed conditions during the flybys.

Backtraced particles are considered to contribute to a decrease in flux, when they impact the surface of Europa or charge exchange with neutrals (from the atmosphere or plume). This is because a backtraced particle that impacts Europa or charge exchanges, does not exist in forward time because neither the atmosphere nor the surface of Europa can be a source of energetic protons. Perturbed fields that cause forbidden regions will cause particles to impact on the surface of Europa in backtracing-sense, which corresponds to an apparent loss from the point of view of the instrument, though in reality it means the particle has been deflected away from the region. In the simulation a particle is considered to have impacted Europa's surface when its trajectory intersects Europa's surface. If the energetic proton charge exchanges, it turns into an energetic neutral atom (ENA) and since it is no longer bound by electromagnetic fields, it escapes the system at a high velocity. The probability of charge exchange with the atmospheric neutrals is determined using Equation 1 from Birdsall (1991).

$$P = 1 - \exp(-n_n \sigma g \Delta t) \tag{1}$$

In Equation 1, n_n is the density of the neutrals at the location of the particle (see following paragraphs), σ is the charge exchange cross-section, g is the relative velocity, and Δt is the time difference between the integration time steps. Because O_2 is thought to be the major constituent of Europa's atmosphere (Plainaki et al., 2018), we use the energy dependant charge exchange cross section of H^+ on O_2 from Basu et al. (1987) for σ. Equation 1 is evaluated at every time step of the particle trajectory. The probability is then compared to a random number between 0 and 1 from a uniform distribution. If the probability exceeds the random value charge exchange is assumed to take place.

For all proton simulations presented in this paper, we apply the analytic description of Europa's atmosphere adopted from Jia et al. (2018). This atmospheric description is also used as input for the MHD simulations discussed in the next section. This description was already used in the study of Huybrighs et al. (2020). Note that in this paper, we describe Europa's atmospheric properties and plasma interaction in a spherical and Cartesian coordinate system centered at Europa. The Cartesian coordinate system is the EPhiO system. The spherical coordinate system is described by the radial distance r, the colatitude θ and the longitude ϕ. θ is measured from the positive z axis and ϕ is measured from the positive y axis in direction of the negative x axis. While the particle tracing internally uses the Cartesian grid, the MHD simulation internally uses the spherical grid. Following Equation 1 from Jia et al. (2018), the density of Europa's molecular oxygen atmosphere (N_n) is larger on the trailing hemisphere than on the leading hemisphere and is prescribed by

$$N_n = \begin{cases} \left(1 + 2\cos\tilde{\phi}\right) \cdot \left[n_{10} \exp\left(\frac{R_E - r}{h_{s1}}\right) + n_{20} \exp\left(\frac{R_E - r}{h_{s2}}\right) \right], & \text{if } \tilde{\phi} \leq 90° \\ n_{10} \exp\left(\frac{R_E - r}{h_{s1}}\right) + n_{20} \exp\left(\frac{R_E - r}{h_{s2}}\right), & \text{if } \tilde{\phi} > 90° \end{cases} \tag{2}$$

where $\tilde{\phi}$ is the azimuthal angle (measured from the negative x axis in EPhiO). The neutral density distribution consists of two exponential functions describing the sublimated component and the sputtered component of the atmosphere with the surface densities n_{10} and n_{20}, and scale heights h_{s1} and h_{s2}, respectively. For further information, the distribution of the neutral number density given in 2 is visualized in Jia et al. (2018), Supplementary, Figure 2.

In the simulation runs with additional plume, we use the analytic description for the density profile of the plume based on Equation 4 from Jia et al. (2018):

$$N_P = N_{P0} \exp\left(\frac{R_E - r}{H_P} - \left(\frac{\tilde{\theta}}{\theta_P}\right)^2 \right) \tag{3}$$

Table 3
Atmospheric Properties Used in the MHD Model

Flyby	n_{10} [m^{-3}]	n_{20} [m^{-3}]	h_{s1} [km]	h_{s2} [km]	N_{P0} [m^{-3}]	H_P [km]	Θ_P [°]	Plume location (θ, ϕ) [°, °]
E17, Case 3–4	1.3×10^{13}	1×10^{12}	100	500	–	–	–	–
E17, Case 5	1.3×10^{13}	1×10^{12}	100	500	2.5×10^{15}	150	15	(180, 180)
E17, Case 6	1.3×10^{13}	1×10^{12}	100	500	–	–	–	–
E25A, Case 3-4	1.0×10^{13}	1×10^{12}	100	500	–	–	–	–
E25A, Case 7	1.0×10^{13}	1×10^{12}	100	500	2.5×10^{15}	150	15	(0, 0)
E25A, Case 8	1.0×10^{13}	1×10^{12}	100	500	–	–	–	–

Note. The parameters are based on Blöcker et al. (2016) and references therein.

The density distribution of the plume has a conical structure and is characterized by the surface density N_{p0}, scale height H_P and opening angle θ_P. $\tilde{\theta}$ is the polar angle measured relative to the central axis of the plume. The atmospheric and plume properties for different flyby scenarios are presented in Table 3.

5. Method: MHD Simulations

The trajectories of the energetic protons can be influenced by inhomogeneities in the electromagnetic field. Therefore, we include the electromagnetic fields from MHD simulations in our particle tracing. The inhomogeneous field takes into account the perturbations in the electromagnetic field resulting from the interaction of Europa's atmosphere with the low energy plasma, including the contribution of plumes. The inhomogeneous fields are obtained from simulations of a three-dimensional magnetohydrodynamic (MHD) model performed on a spherical grid. MHD is a suitable approach to describe the interaction of the cold magnetospheric plasma with Europa's atmosphere since the gyroradius and the period of cyclotron motion of the plasma particles are smaller than the typical length and time scales of the interaction. The MHD model we used was applied in previous studies to investigate the influence of atmospheric inhomogeneities on Europa's plasma interaction (Blöcker et al., 2016) and the effect of atmospheric asymmetries on Io's plasma interaction with Jupiter's magnetosphere (Blöcker et al., 2018, 2020). The model results were also applied in the recent study of depletions of energetic protons during Galileo flyby E26 by Huybrighs et al. (2020). The applied MHD model for Europa's plasma interaction is described in detail in Blöcker et al. (2016). This model is a modified version of the ZEUS-MP MHD code (Hayes et al., 2006; Norman, 2000) and solves a set of 3D MHD equations in spherical coordinates. The set of equations takes into account collisions between ions and neutrals, electron impact ionization, dissociative recombination, and electromagnetic induction in a subsurface water ocean. Consistent boundary conditions at a nonconducting surface derived by Duling et al. (2014) were used in the model.

For all MHD simulations presented in this paper, we apply the analytic description of Europa's atmosphere described in Section 4. The atmospheric and plume properties for different flyby scenarios are presented in Table 3. The initial and boundary condition values for the simulations of the Galileo flybys are summarized in Table 4. The simulation domain extends to $20R_E$ from Europa's center in radial direction. The resolution in radial direction increases by a factor of 1.015 for the E17 flyby simulations (1.01 for the E25A flyby simulations) from cell to cell from $\Delta r = 13$ km ($\Delta r = 30$ km for the E25A flyby simulations) close to Europa's surface and to $\Delta r = 450$ km ($\Delta r = 320$ km for the E25A flyby simulations) at the outer boundary. The resolution of the grid in angular direction is equidistant with $\Delta \theta = 1.5°$ and $\Delta \phi = 3°$. For the proton simulations the output of the MHD simulations are interpolated at a resolution 0.03 R_E (~47 km) for E17 and a resolution of 0.025 R_E for E17 (~40 km).

The resolution of the interpolated MHD simulation (40–47 km) used in the particle tracing is larger than the gyroradii of particles with pitch angles below 30° (Figure B1), meaning that these particles will not experience gradients along their gyromotion and experience no drift. However, as we will show,

Table 4
Initial and Boundary Condition Values in the EPhiO System for the MHD Model

Flyby	n^a [cm^{-3}]	v [km/s]	B [nT]	e^b [nPa]
E17	94	(104, 0, 0)	(73, −100, −425)	1.97
E25A	47	(104, 0, 0)	(−7, −209, −382)	0.98

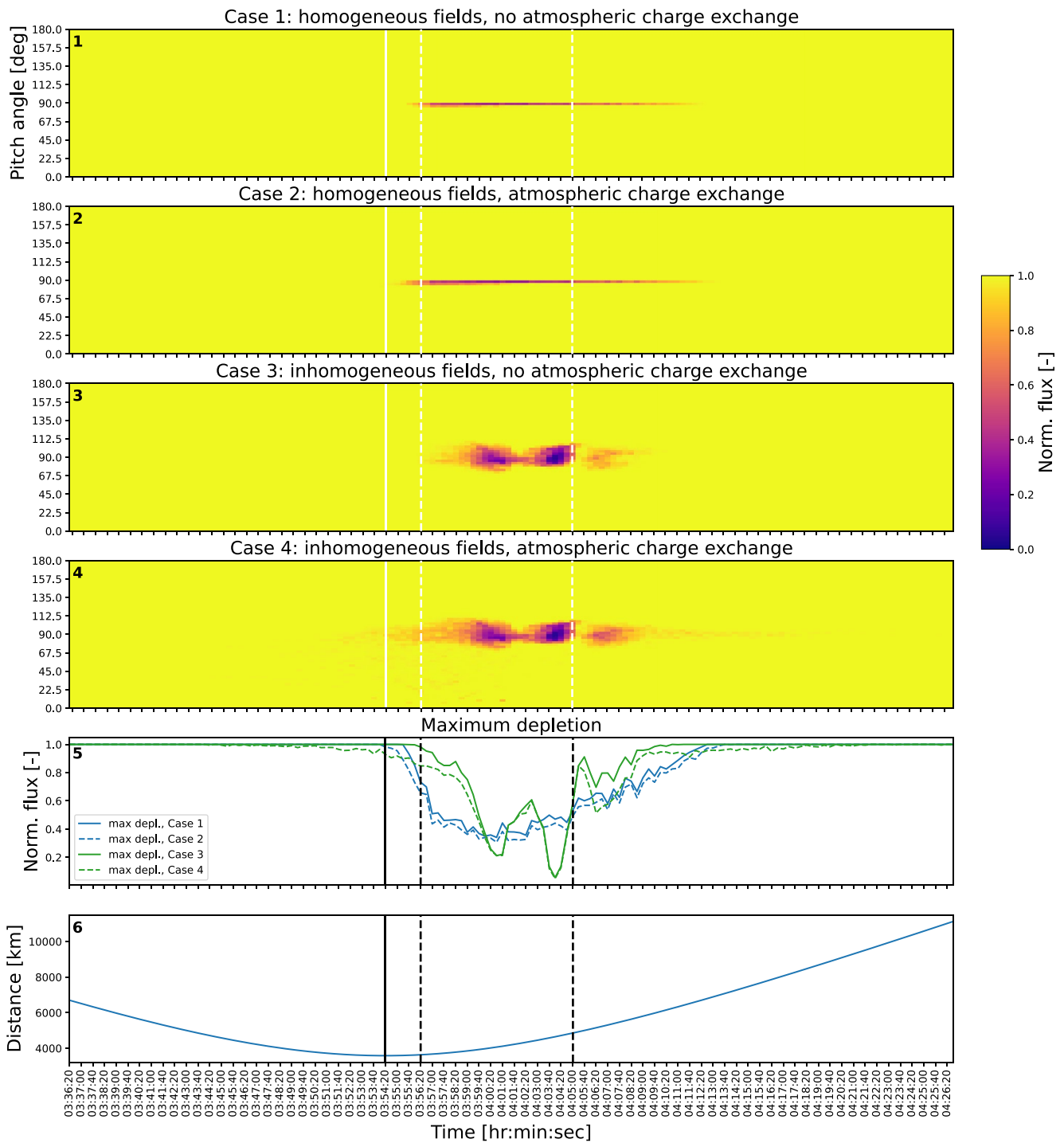[a]Magnetospheric plasma number density. [b]Internal energy density.

Figure 4. Simulations for the E17 flyby, TP1 channel (80–220 keV protons). Note in particular the differences between the simulations for the homogeneous fields (Panels 1–2) and inhomogeneous fields (Panels 3–4). The fifth panel shows the deepest depletion seen at any of the pitch angles at each time step of the simulations. The sixth panel shows a comparison between simulations and data. The bottom panel shows the radial distance to Europa. The solid vertical line indicates the closest approach. The dashed vertical lines indicate the time of the encounter with the Alfvén wing, as discussed in Appendix D.

because the predicted depletion appears to be confined closer to the 90° pitch angle and already disappears at higher angles than 30°, we do not expect this to cause a major difference in the simulated depletion (Figure 4).

Results of the MHD simulation and a comparison with the MAG data can be found in Appendix D. Although the MHD simulation results shown here are produced with the atmospheric model described in Section 4, the

results are very similar to those from the MHD model with a radially symmetric atmosphere presented by Blöcker et al. (2016). A more detailed discussion of the comparison between the E17 and E25A MHD simulations and the magnetic field measurements can be found in Bloecker et al., 2016.

6. Results and Discussion

In the following sections we will first simulate the proton dropouts under the scenarios described in Section 3. Subsequently we will reproduce the measurement from the simulations and compare this reproduction to the Galileo measurements.

6.1. The Alfvén Wings and Ionospheric Field Perturbations Widen the Pitch Angle Spread of Losses Along the Trajectory

In this section we will demonstrate that due to the presence of the field perturbations of the Alfvén wings and the ionosphere the pitch angle range over which protons are depleted will widen and a complex depletion structure with localized dropouts along the spacecraft trajectory will form, compared to the case with homogeneous fields for which the depletion is focused on a narrow pitch angle range without finer structure. Near the edges of the wing encounter perturbed fields will also reduce the time over which the depletions will be observed, as compared to the case with homogeneous fields. We demonstrate the above by comparing the simulation with homogeneous fields (Cases 1 and 2) to those with inhomogeneous fields (Cases 3 and 4).

We observe differences in the modeled pitch angle distribution of the depletion and the depth of the depletion between the simulations with homogeneous fields (Cases 1 and 2) and inhomogeneous fields (Cases 3 and 4) for both flybys. Cases 1–4 are shown in Panels 1–4 in Figure 4 (E17, TP1: 80–220 keV), Figure 5 (E17, TP2: 220–540 keV), Figure 6 (E25A, TP1: 80–220 keV) and Figure 7 (E25A, TP2: 220–540 keV).

The depletions in the homogeneous cases are focused on a narrow pitch angle zone at the 90° pitch angle. The depletion structure is also monotonous and has no particular structure and lasts for the entire duration during which the Alfvén wing is encountered in the magnetic field data (indicated by the dashed white lines). The occurrence of depletions in Case 1 (no charge exchange) means that for these particular pitch angles the trajectories of the particles intersect with the surface of Europa in the back-tracing sense, and can therefore not exist. In the forward sense it means that particles near the 90° pitch angle cannot reach the EPD detector because they are blocked by Europa's surface. The depletions we see in Case 1 can thus be entirely attributed to absorption by Europa's surface.

In the inhomogeneous cases the depletion extends over a wider pitch angle range (about 20° for E17). Furthermore, the maximum depth of the depletion along the trajectory is deeper in the inhomogeneous cases for both E17 and E25A than for the homogeneous case. The trajectory of a single energetic proton backtraced during flyby E17 is shown in Figure 8 to illustrate the difference between the homogeneous (Cases 1–2) and inhomogeneous cases (Cases 3–4). With homogeneous fields (no Alfvén wings or other field perturbations) the particle escapes to higher magnetic latitude without encountering Europa (top panels). With inhomogeneous fields (Alfvén wings and ionospheric perturbations present) the energetic protons will experience gradients in the magnetic field that result in gradient drifts which modify the trajectories of the protons. Energetic protons with a pitch angle close to 90° mirror locally due to local maxima in the field and eventually impact Europa (bottom panels). Pitch angles away from 90° have enough field-aligned velocity to mirror far from Europa and do not interact with the moon at all. Note that when the particle impacts in the backward sense, due to field perturbations, it means that in the forward sense this particle cannot exist because Europa is not a source of energetic protons, and hence it should be registered as depleted. Effectively, a forbidden region is created by the perturbed fields in which the energetic protons have been deflected away.

The deflections are caused by gradients in the magnetic field. The gradients experienced by the backtraced particles are not solely attributable to the Alfvén wings, in particular closer to Europa field perturbations associated with the ionosphere occur. Inside the Alfvén wings described theoretically in Neubauer (1980) the field magnitude should be constant. However, in the simulations field perturbations associated with the ionosphere occur up to several Europa radii away from the moon. During flyby E17, perturbations in the field magnitude on the order of 15nT are present which implies that the plasma interaction is not purely Alfvénic, and that both, Alfvénic
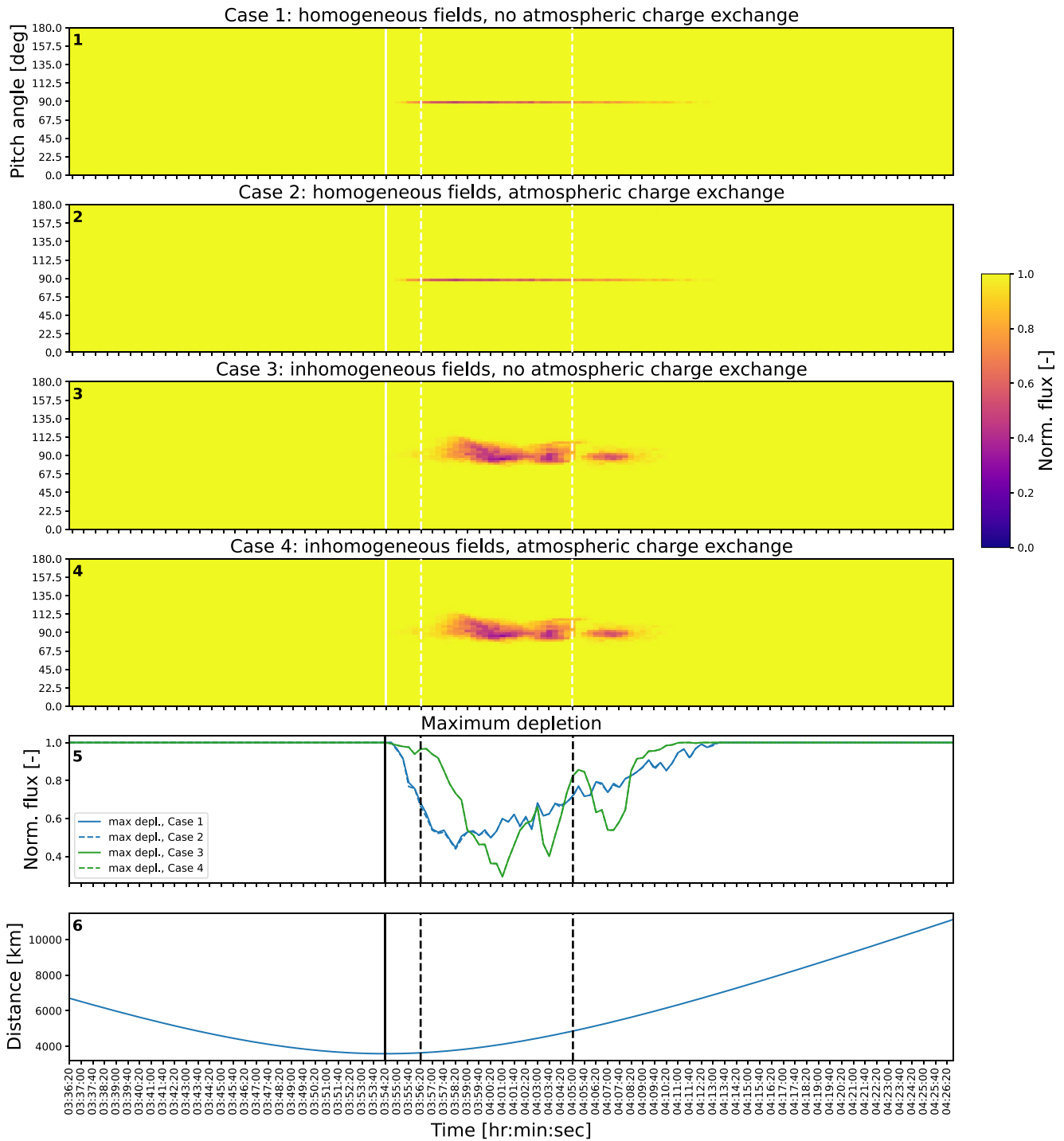
Figure 5. Simulations for the E17 flyby, TP2 channel (220–540 keV protons). Note in particular the differences between the simulations for the homogeneous fields (Panels 1–2) and inhomogeneous fields (Panels 3–4). The fifth panel shows the deepest depletion seen at any of the pitch angles at each time step of the simulations. Note that there is no difference between Case 1 and 2, and Case 3 and 4 respectively due to the decrease in charge exchange cross section compared to TP1. The bottom panel shows the radial distance to Europa. The solid vertical line indicates the closest approach. The dashed vertical lines indicate the time of the encounter with the Alfvén wing, as discussed in Appendix D.

and ionospheric, currents alter the magnetic field environment. However, for flyby E25A, during which we also simulate a complex pattern of depletion, no field magnitude perturbations occur along the spacecraft trajectory in the simulation due to the larger distance to Europa, the simulated environment is therefore a purely Alfvénic one.
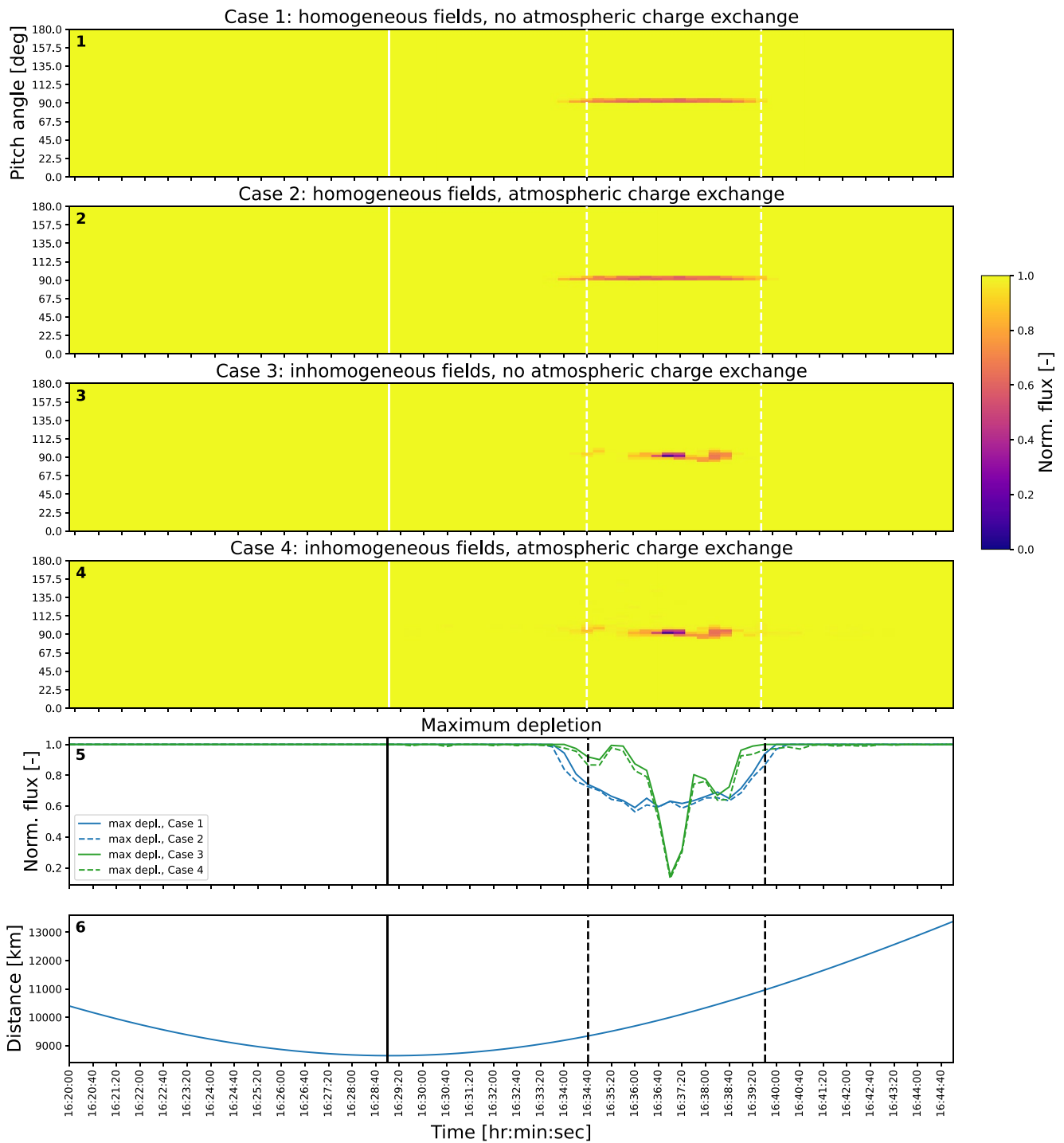
Figure 6. Simulations for the E25A flyby, TP1 channel (80–220 keV protons). Note in particular the differences between the simulations for the homogeneous fields (Panels 1–2) and inhomogeneous fields (Panels 3–4). The fifth panel shows the deepest depletion seen at any of the pitch angles at each time step of the simulations. The bottom panel shows the radial distance to Europa. The solid vertical line indicates the closest approach. The dashed vertical lines indicate the time of the encounter with the Alfvén wing, as discussed in Appendix D.

Thus, since the particles can also traverse regions of mixed-origin field perturbations (with both perturbations due to the Alfvén wings and ionospheric perturbations mapped along the wing) or environments nearer the moon (where Alfvén wing perturbations are not dominant) it is the global field structure, and not exclusively the "pure" Alfvén wing perturbations, that explains the precise structure of the measured proton losses.
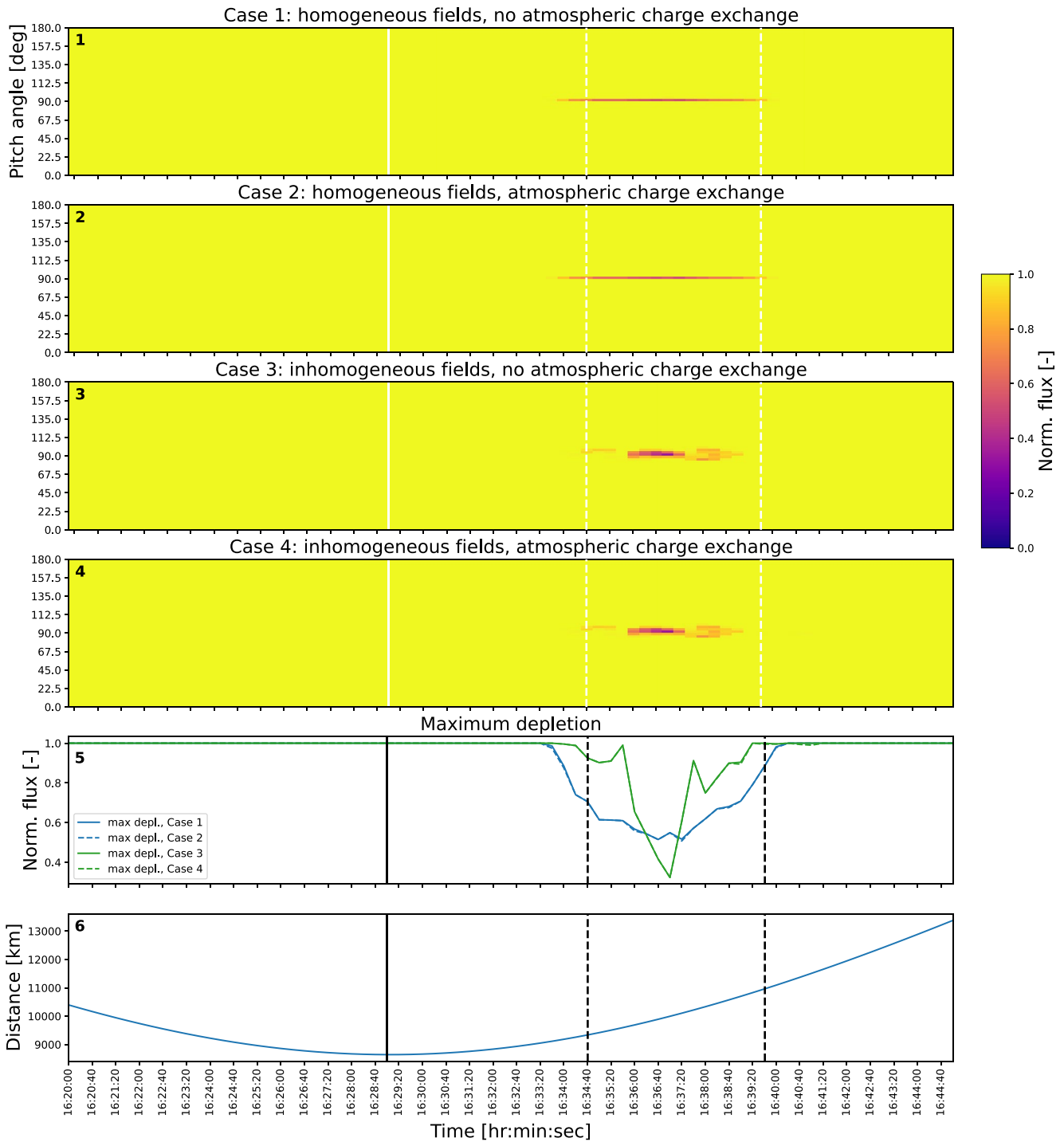
Figure 7. Simulations for the E25A flyby, TP2 channel (220–540 keV protons). Note in particular the differences between the simulations for the homogeneous fields (Panels 1–2) and inhomogeneous fields (Panels 3–4). The fifth panel shows the deepest depletion seen at any of the pitch angles at each time step of the simulations. Note that there is no difference between Case 1 and 2, and Case 3 and 4 respectively due to the decrease in charge exchange cross section compared to TP1. The bottom panel shows the radial distance to Europa. The solid vertical line indicates the closest approach. The dashed vertical lines indicate the time of the encounter with the Alfvén wing, as discussed in Appendix D.
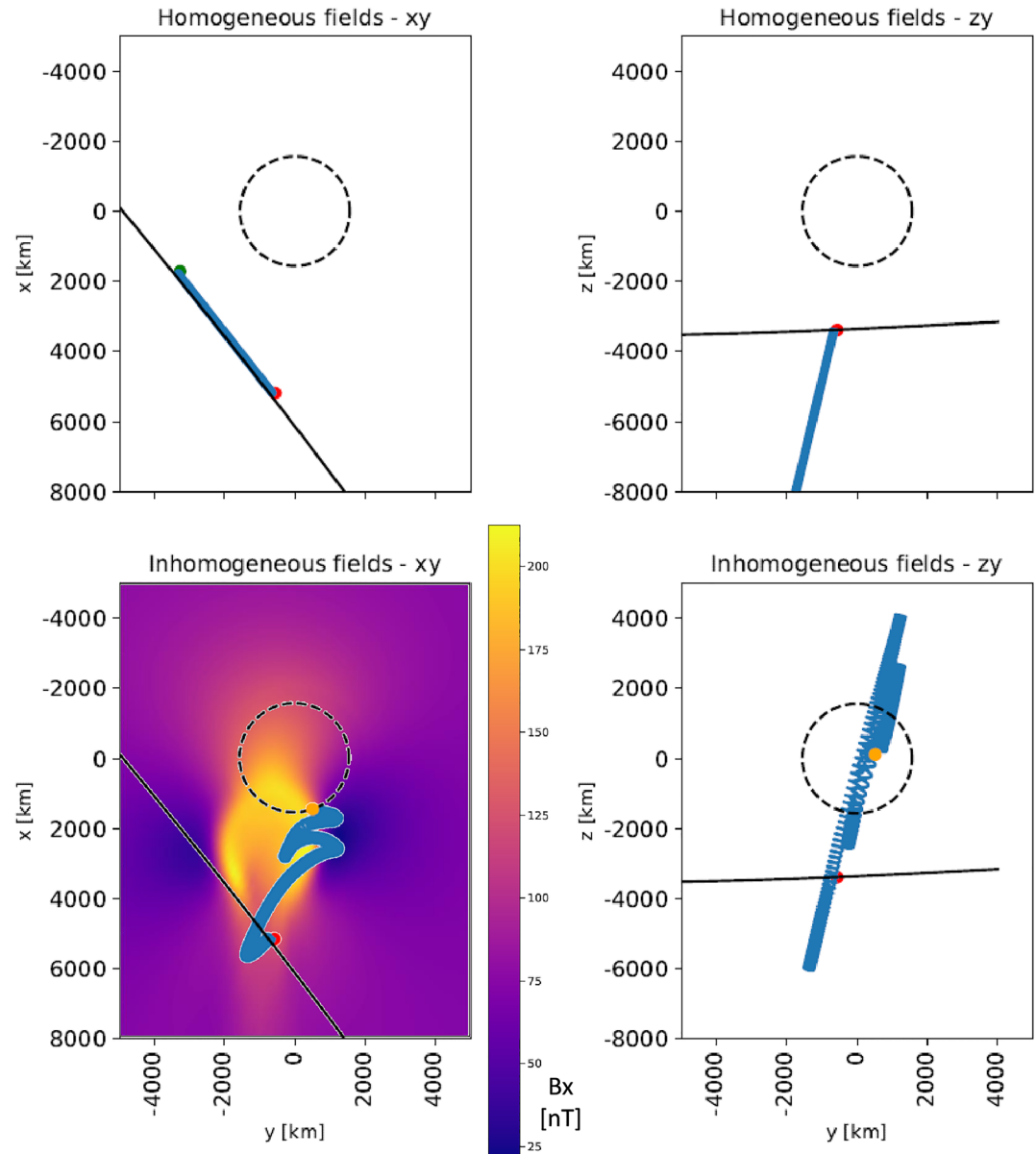
Figure 8. The trajectory of a 100 keV proton launched from the same location (red point) along the E17 trajectory (solid black line) using the same pointing vector, without perturbed fields (top) and with perturbed fields (bottom). With homogeneous fields (no Alfvén wings or ionospheric perturbations) the particle escapes and does not interact directly with Europa. The final point of the simulated trajectory is indicated by the green point. With inhomogeneous fields (Alfvén wings and ionospheric perturbations present) the particle mirrors locally and impacts Europa (orange point). In the background of the bottom left panel the Bx component (in nT) of the simulated perturbed fields is also shown, the corresponding z-coordinate of the XY slice is −3,500 km (at the starting point of the particle). Note that the position of the Alfvén wing shifts for different z coordinates. The *x*-axis is along the direction of the magnetospheric plasma flow, the *z*-axis is parallel to Jupiter's spin axis, and the *y*-axis is facing Jupiter.

Furthermore, we also observe that the structure of the pitch angle distribution along the trajectory is different between the 80–220 keV (Figure 4) and 220–540 keV range (Figure 5), we attribute this to the difference in energy and gyroradius of the respective protons. Both the energy and gyroradius affect the drift motion resulting from gradients in the magnetic field.

In the inhomogeneous case the structure of the depletion as a function of pitch angle along the trajectory is complex rather than monotonous. In particular for E17 we observe a double maximum of the depletion, while in

E25A we observe a pronounced maximum of the depletion. The maximum depletion occurring at each time step in the pitch angle range of 0–180° is shown in Panel 5 of Figures 4–7. Even though the structure of the depletions as a function of pitch angle are similar between the flybys in the homogeneous case, that is, monotonous and concentrated along the 90° pitch angle, the structure of the depletion is different between the two flybys in the inhomogeneous case. This implies that the structure depends on the specific magnetic field gradients traversed by the energetic protons, which cause drifts in their motion and thereby determine which particles deplete. We also observe that the depleted region along the trajectory is of a shorter duration for the inhomogeneous case than for the homogeneous case. For TP1 (Figures 4 and 6) this reduction in time is visible in all cases for both flybys with inhomogeneous fields and no charge-exchange. The shortening is also apparent for the TP2 channel for both flybys (Figures 5 and 7) where little atmospheric charge exchange occurs (the effect of charge exchange is discussed in more detail in Section 6.2). For those times where the depletion is no longer present, compared to the case with homogeneous fields, the perturbed fields guide the backtraced proton in such a way that it no longer impacts on Europa's surface. In forward sense we can thus consider this particle as being deflected away from Europa's surface.

Lastly, we do not attribute the depletion inside the Alfvén wings due to a deflection of the plasma flow around them. The energetic protons in our simulations have speeds exceeding 4,000 km/s (80keV proton). This is an order of magnitude larger than the corotational plasma flow (104 km/s). Any deflections away from the corotational direction are a fraction of this. The energetic protons will thus traverse the Alfvén wings cross section (approximately 2 R_E) before any flow deflection will have a significant effect.

In general, we find that the inhomogeneous fields associated with the Alfvén wings and the ionosphere have a significant effect on the depletion by widening the pitch angle distribution of the depletion and creating a more complex depletion structure. Whereas in the homogeneous cases the depletion is confined to a narrow pitch angle range and has no structure, in the inhomogeneous cases the depletion has a complex dependence on the pitch angle and has a complex structure with multiple local maxima of depletion.

6.2. Effect of Charge Exchange With Europa's Atmosphere Minor Compared to Inhomogeneous Fields

The effect of atmospheric charge exchange can be determined by comparing the depletions in Panel 1 with Panel 2, and Panel 3 with Panel 4 in Figures 4–7. The difference can also be observed by comparing the maxima of the depletion in Panel 5 of these figures. We find that only at the 80–220 keV energy range there is a contribution due to charge exchange. In both Cases 2 and 4 for E17 and E25A the addition of atmospheric change introduces an extended depletion near the 90° pitch angle. The depth of the depletion is less than 10%. The effect of atmospheric charge exchange effectively increases the size of Europa as an obstacle for the energetic protons. Note that this extension only occurs in the at 80–220 keV range and not at 220–540 keV due to the reduced charge exchange cross section. This supports previous studies such as Huybrighs et al. (2020) and Addison et al. (2021) that reported that energetic protons of energies around 100 keV can, at least partially, be depleted by charge exchange with atmospheric neutrals. However, we find that for these particular flybys the additional contribution to the depletion due to atmospheric charge exchange is minor in comparison to the contribution of the inhomogeneous fields. We consider that the contribution due to atmospheric charge exchange is unlikely to be picked up, even for very high resolution measurements.

6.3. Effect of Plumes on the Depletions Is Minor Compared to the Overall Depletion Structure Due To the Field Perturbations

Blöcker et al. (2016) have demonstrated that atmospheric inhomogeneities near the North and South pole cause north-south asymmetries in the Alfvén wings. Here we show that the asymmetries affect the maximum depth of the proton depletions, but that the effect is minor compared to the overall depletion associated with the field pertubations during E17 and E25A.

For flyby E17 (Figure 9) we consider Case 5 (Panel 2) with a plume at the south pole ($\theta = 180°$, $\phi = 180°$). For Flyby E25A we consider a plume on the north pole (Case 7, Panel 2 in Figure 10).

For E17 the main difference between the default Case 4 and the plume case (Case 5) is the maximum depth of the depletion. A minor difference can be observed from the line plots in Panel 4 of Figure 9. These line plots show
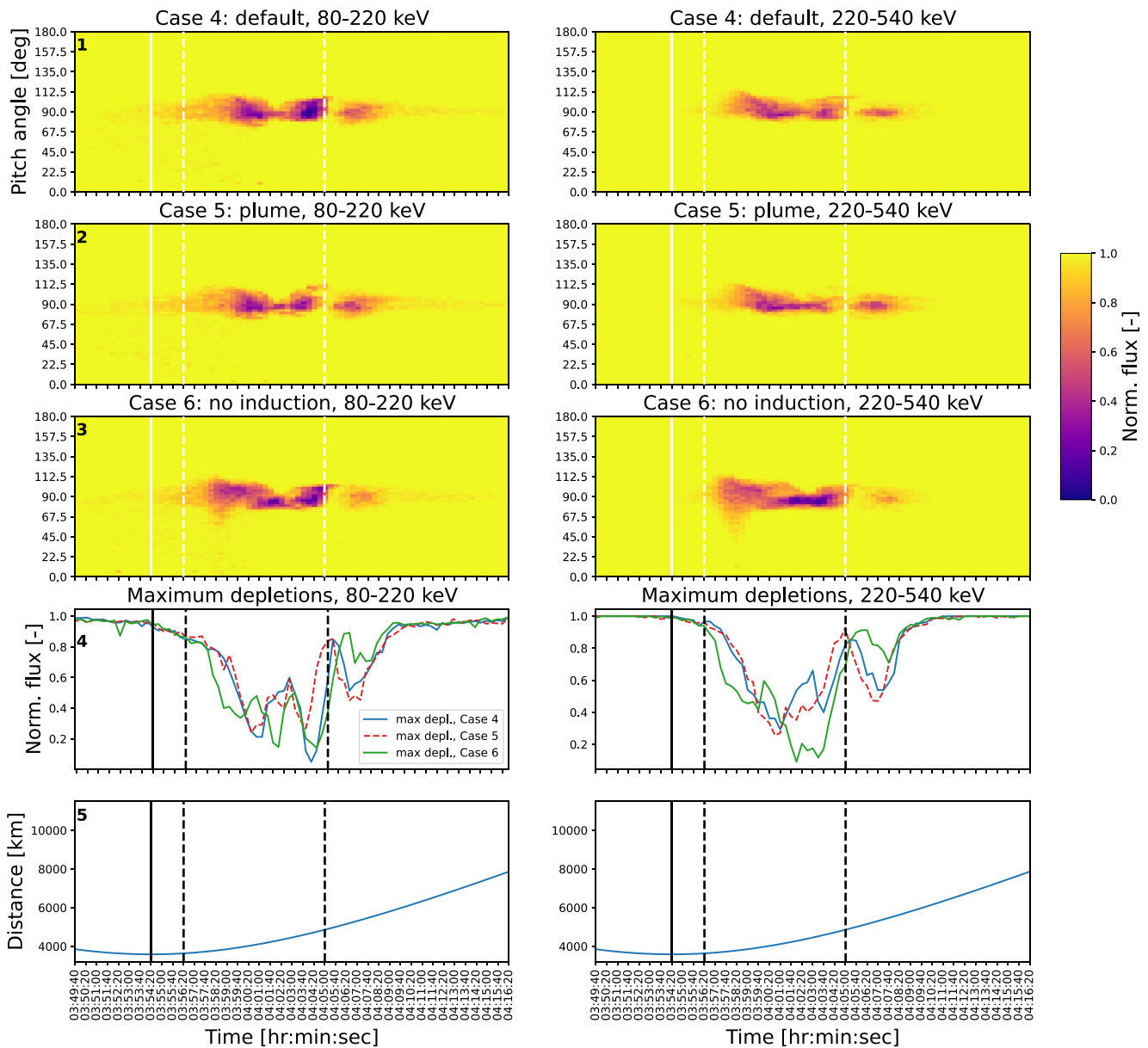
Figure 9. Simulations for the E17 flyby, TP1 channel (80–220 keV protons) on the left and TP2 channel (220–540 keV protons) on the right. Note in particular the differences between the default case (Case 4, top panel) and the case without induced dipole (Case 6 third panel). The fourth panel shows the maximum depletion seen at any of the pitch angles at each timestep in the simulations. The last panel shows the distance to Europa. The solid vertical line indicates the closest approach. The dashed vertical lines indicate the time of the encounter with the Alfvén wing, as discussed in Appendix D.

the maximum depth of depletion seen at any of the pitch angles at each time step. There is no notable difference in the structure of the pitch angle distribution of the depletions.

For E25A (see Figure 10) in the TP2 channel a decrease in the maximum depth of the depletion can be observed by comparing the default case (Case 4, Panel 1) with the plume case (Case 7, Panel 2). In addition, at the lower energies (80–220 keV) there are minor differences in the maximum depth of depletion over the pitch angle range along the trajectory, which can be observed in Panel 4.

Thus, overall the effect of the plumes located at the North/South pole on the depletions is limited to changes in the maximum depth of the depletion and minor compared to the depletion structure of the perturbed fields. We consider it unlikely that the presence of a plume could be determined solely from the energetic proton measurements made during the Alfvén wing encounters in flyby E17 and E25A. We attribute the relatively minor
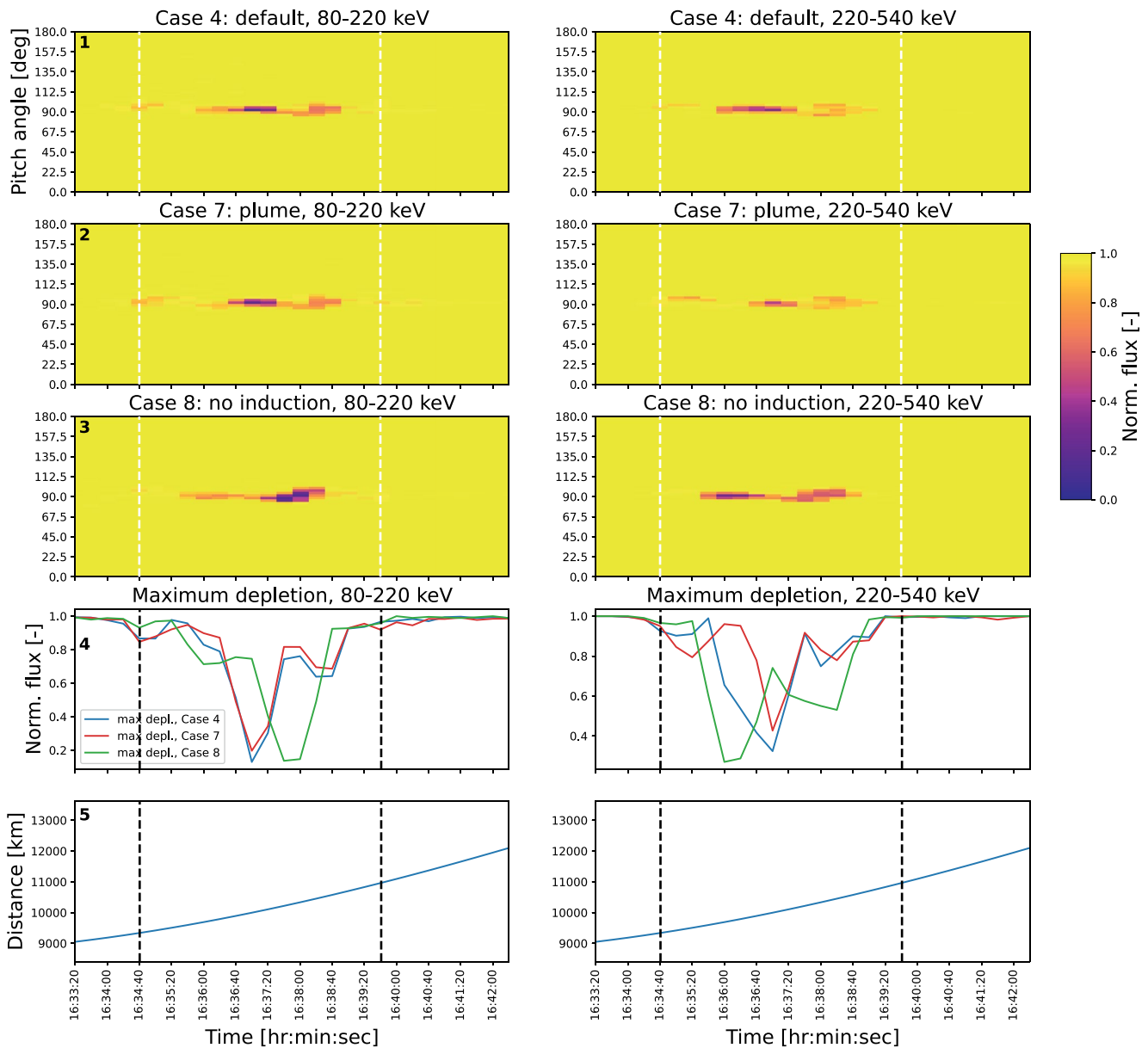
Figure 10. Simulations for the E25A flyby, TP1 channel (80–220 keV protons) on the left and TP2 channel (220–540 keV protons) on the right. Note in particular the differences between the default case (Case 4, top panel) and the case without induced dipole (Case 8 third panel). The fourth panel shows the maximum depletion seen at any of the pitch angles at each timestep in the simulations. The last panel shows the distance to Europa. The solid vertical line indicates the closest approach. The dashed vertical lines indicate the time of the encounter with the Alfvén wing, as discussed in Appendix D.

effect of the plumes on the proton losses to the relatively small effect of the plumes on the magnetic field during these two flybys. The plume changes the magnetic field environment in the Alfvén wings, this can be seen in Figure D1. But, neither flyby E17 or E25A went through the core region of the Alfvén wings, as discussed in Section Appendix D. Therefore, for both E17 and E25A the difference in the magnetic field along the trajectory between with and without plume is very small (see Figure 12 in Panel 4–6). We consider that the effect of the plume depends on the flyby geometry, we cannot exclude that flybys that pass through a section of the Alfvén wings where the Alfvén winglet are more pronounced could experience a more pronounced effect on the protons due to the plume winglet.

Furthermore, we cannot exclude that plumes with larger densities or different structures could have a more pronounced effect on the depletion. The effect of the plumes on the fields in the Alfvén wings will increase

with increasing plume density. The plume density N_{P0} considered here is 2.5×10^{15} m^{-3}. Larger densities are indeed possible, for example, Jia et al. (2018) inferred a plume density of 3.9×10^{15} m^{-3}. Furthermore, the effect of the plume on the field perturbations depends on the shape of the plume. Blöcker et al. (2016) consider a plume during E17 at $\theta = 140°$, $\phi = 290°$, using a wider plume based on Roth et al. (2014), rather than the conical plume used in this study. We found that running a MHD simulation for a denser plume at the same location, but using the conical description from Jia et al. (2018), has a weaker effect on the field. Though the effect of the later case on the proton depletions is minor, we expect that the effect of broader plumes on the depletions will be larger, in particular at higher densities. A wider investigation of the plume parameter space is needed to establish which configurations would have the most effect on the depletions, and if those effects are detectable.

6.4. Induced Dipole Modifies the Pitch Angle Distribution of Proton Losses Along the Alfvén Wings During Distant Flybys

Neubauer (1999) demonstrated that the induced dipole related to the subsurface ocean affects the Alfvén wings resulting in a shrinkage and displacement of the wings. In this section we consider the effect of the induced dipole on the proton depletions in the Alfvén wings. We will show that the structure of the pitch angle distribution along the spacecraft trajectory is altered by the induced dipole.

Case 6 (Panel 3) and Case 8 (Panel 3) in Figures 9 and 10 show, respectively, the simulated depletion near the Alfvén wing encounter, for which the effect of the induced dipole on the depletion has been neglected. Case 4 in Panel 1 in both figures shows the default case (inhomogeneous fields and atmospheric charge exchange). The default cases are also shown in Panel 4 in Figures 4 and 5 for E17 and in Figures 6 and 7 for E25A.

For E17 (Figure 9, Panel 3) we find that the lack of an induced dipole alters the pitch angle distribution of the depletion compared to the default case (Panel 1). Near 04:02:20 a third maximum of depletion appears, while in TP2 the depletion is enhanced in the second half of the Alfvén wing encounter.

For E25A (Figure 10) we find that the lack of an induced dipole shifts the point of the maximum depletion in both energy channels. The difference in the proton depletions between the dipole/no-dipole case is larger for E25A compared to E17. At larger magnetic latitudes the contribution to the field of the induced dipole is larger, and therefore also the shrinkage and displacement of the Alfvén wings (Neubauer, 1999). Indeed, for E25A the magnetic latitude is 9.9° and for E17 it is 3.6° (Volwerk et al., 2007). Figure 12 (Panels 4–6) shows the difference in the fields along the trajectory for the simulation with and without dipole.

We conclude that the effect of the induced dipole on the proton depletions in the Alfvén wings is not negligible even during distant flybys. Therefore, the proton depletions could in principle be used as an additional way to provide evidence for an induced dipole at Europa, but possibly also at other moons which show a sub-Alfvénic interaction with the magnetospheric plasma environment.

6.5. Inhomogeneous Simulations Agree Qualitatively Better With Data

In this section we suggest that the inhomogeneous fields provide for a qualitative better description of the data than the homogeneous cases. We will show that whereas in the homogeneous case no significant depletion would appear in the simulated the measurement, the simulated measurement for the inhomogeneous case will show a complex structure of depletion along the sky with local maxima of depletion, similar as for the data. Furthermore, we will argue that to gain confidence in our interpretation of the magnetic field, a well reconstructed energetic proton (and ion) flux is important.

Figure 11 shows a comparison between the simulations for flyby E17 and the data. We compare the data, row 1 for 80–220 keV (TP1) and row 4 for 220–540 keV (TP2), with the simulations for homogeneous fields (Case 1, row 2 and 6) and inhomogeneous fields (Case 2, row 3 and 7). We simulated the three skymaps around the center time in Figure 2, which are the skymaps in which the depletions are most apparent.

The simulations have been made by reproducing the pointing of the EPD instrument, the sectoring of the data and the averaging over two cycles. To allow optimal comparison with the data the simulations are also represented as skymaps. Further technical details relevant to the reconstruction of the measurement are provided in Appendix E.
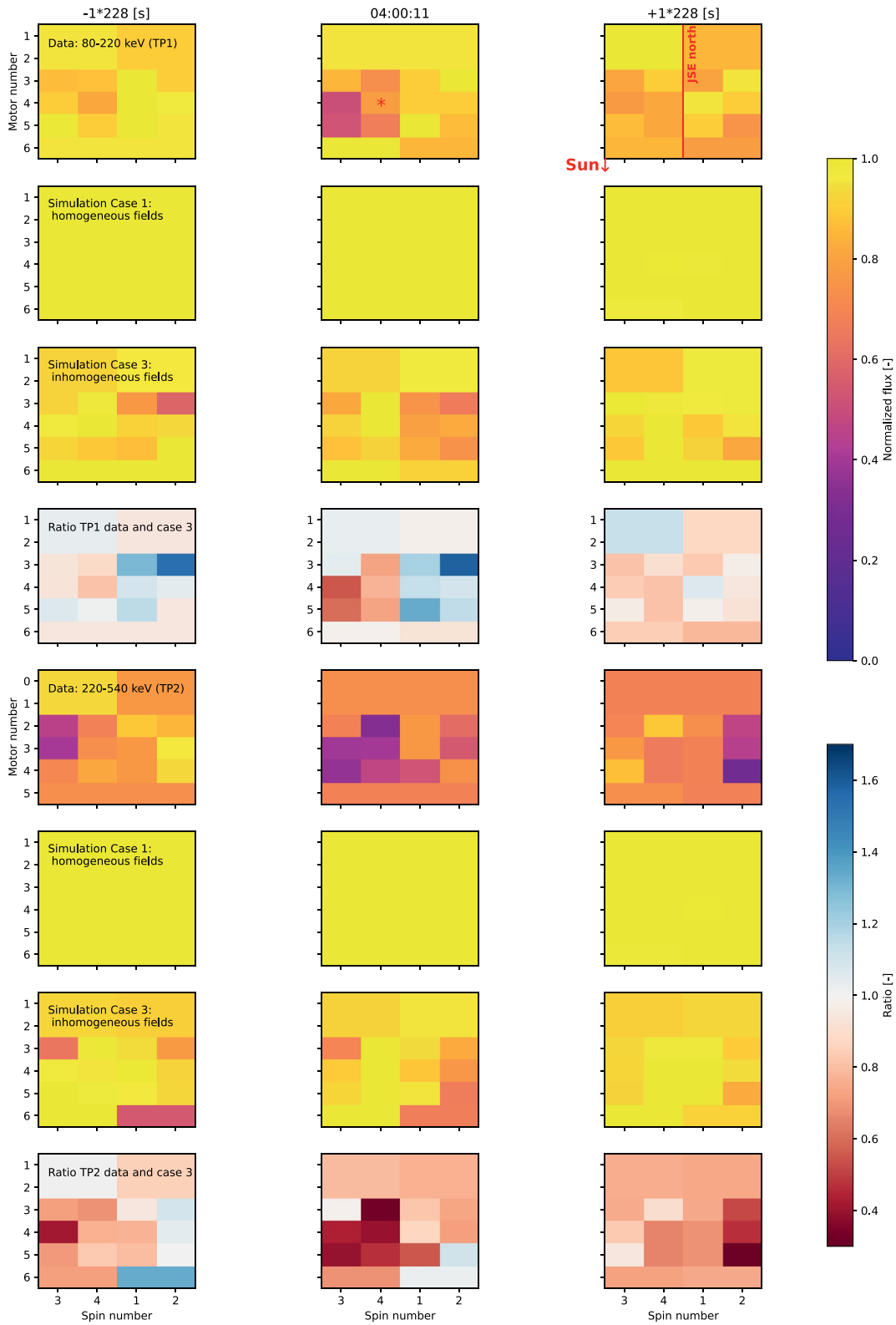
Figure 11.

First we observe that for the homogeneous cases at both energy channels (panels 2 and 6) no significant depletions are predicted. The skymaps averaged over two cycles remain essentially unaltered. This means that the narrow (in pitch angle) depletion feature predicted in the simulations with homogeneous fields shown in panels 1 and 2 in Figures 4 and 5 do not translate to a significant change in the measurement, as a consequence of the instrument pointing, sectoring and averaging. Thus, in the homogeneous model we would not expect any significant change in the proton distribution to occur in these three skymaps, compared to the skymaps before or after the encounter. This suggests that the model with homogeneous fields cannot explain the measured depletions.

In contrast to the homogeneous case we observe that the inhomogeneous cases (panel 3 and 7) predict a complex structure of depletions over the sky, with localized maxima of depletion. Thus, in the inhomogeneous model we expect significant changes in the proton distribution to occur in these three skymaps, compared to the skymaps before or after the encounter. However, discrepancies between the simulations and the data remain. Specifically, the maximum of the depletion is larger in the data in all cases, the maxima of the depletion do not coincide in the same sectors in column 1 and 2 and there are sectors which are depleted in the data, but not in the simulation. These discrepancies illustrate that the agreement between the simulations with inhomogeneous fields is improved, but not complete. Likely causes of the discrepancies are discussed in the following paragraphs. Even though these discrepancies are visible between the inhomogeneous cases and the data, we conclude that there is a better qualitative agreement between the inhomogeneous case and the data, in the sense that the inhomogeneous case shows a complex distribution of the proton losses with local maxima of depletion. This better qualitative agreement suggests that the perturbed fields associated with the Alfvén wing and ionosphere play an important role in the proton losses observed during the Alfvén wing encounters. The lack of significant depletion in the skymap for the homogeneous case, suggests that the narrow (in pitch angle) depletion region is unlikely to show up in measurements that do not show the full pitch angle range. The contribution of the perturbed fields on the proton dropouts is therefore a measurable effect. Thus, any dropout present in the skymaps is suggestive of the presence of an Alfvén wing.

For E25A we also observe that discrepancies between the simulation and the data occur. The simulation essentially predicts no depletion after the exit of the Alfvén wing (16:39:48), see Figures 6 and 7. However, the data suggest that localized depletions are still taking place after the wing exit. This is apparent in Figure 3 in column 4, which contains measurements taken after the wing exit. However, due to the uncertainty of the LGA data it cannot be determined where in the 342 s timeframe these depletions were measured. Note that we do not provide a skymap simulation for flyby E25A. For flyby E25A the data are averaged from three instrument cycles (or equivalently, three sky maps) and thus provides less information than E17, during which the data is averaged from two cycles. The averaging of three skymaps further complicates the interpretation of the measurement. Therefore, we don't expect that a comparison for E25A will reveal any additional details. Further technical details on the reproduction of the pointing during flyby E25A can be found in Appendix E.

The poor spatial and temporal resolution of the EPD LGA data prevents us from isolating any depletion features related to the induced dipole or atmospheric charge exchange. Neither is the effect of the simulated plumes large enough for its presence to be established in the data. Overall, it appears that the close flybys are more suitable to detect depletion features related to atmospheric charge exchange or plumes, because of the larger effect of charge exchange with neutrals close to the moon, as demonstrated in Huybrighs et al. (2020, 2021).

We propose that discrepancies between the simulated electromagnetic fields and the real situation could be the source of the discrepancy between the simulated proton depletions and the measurements. As we demonstrated in the previous sections the dropouts are sensitive in changes of the field structure in the Alfvén wings, for example,

Figure 11. Comparison between data, row 1 for 80–220 keV (TP1) and row 5 for 220–540 keV (TP2), with the simulations for homogeneous fields (Case 1, row 2 and 6) and inhomogeneous fields, Case 2 row 3 and 7. Darker colors represent the depletions. Rows 4 and 8 represent the ratio of the data and the inhomogeneous simulations. Whereas the simulations with homogeneous fields produce no significant depletion, the simulations with inhomogeneous fields (and Alfvén wings) produce a complex depletion structure, suggesting a better qualitative agreement with the data. The panels represent skymaps that are composed of 16 sectors which have been averaged during two instrument cycles lasting 228 s in total. During each cycle the sky was scanned once. The starting time of the middle panel is indicated above the panel. The starting time of the other panels are expressed relative to the middle one. The red star in the top-middle panel indicates the sector closest to Europa, during the composition of the first of the two skymaps that have been averaged onboard the spacecraft to obtain the middle panel. EPD skymaps are provided in the JSE frame (Jovicentric Solar Ecliptic), JSE north and the direction of sun are indicated in the top right panel. The horizontal axis represents the spin axis, where the spin number indicates the order of measurement. The vertical axis represents the axis scanned by moving the EPD motor over positions 1 to 6. A detailed description about how the skymap is composed can be found in Appendix E.
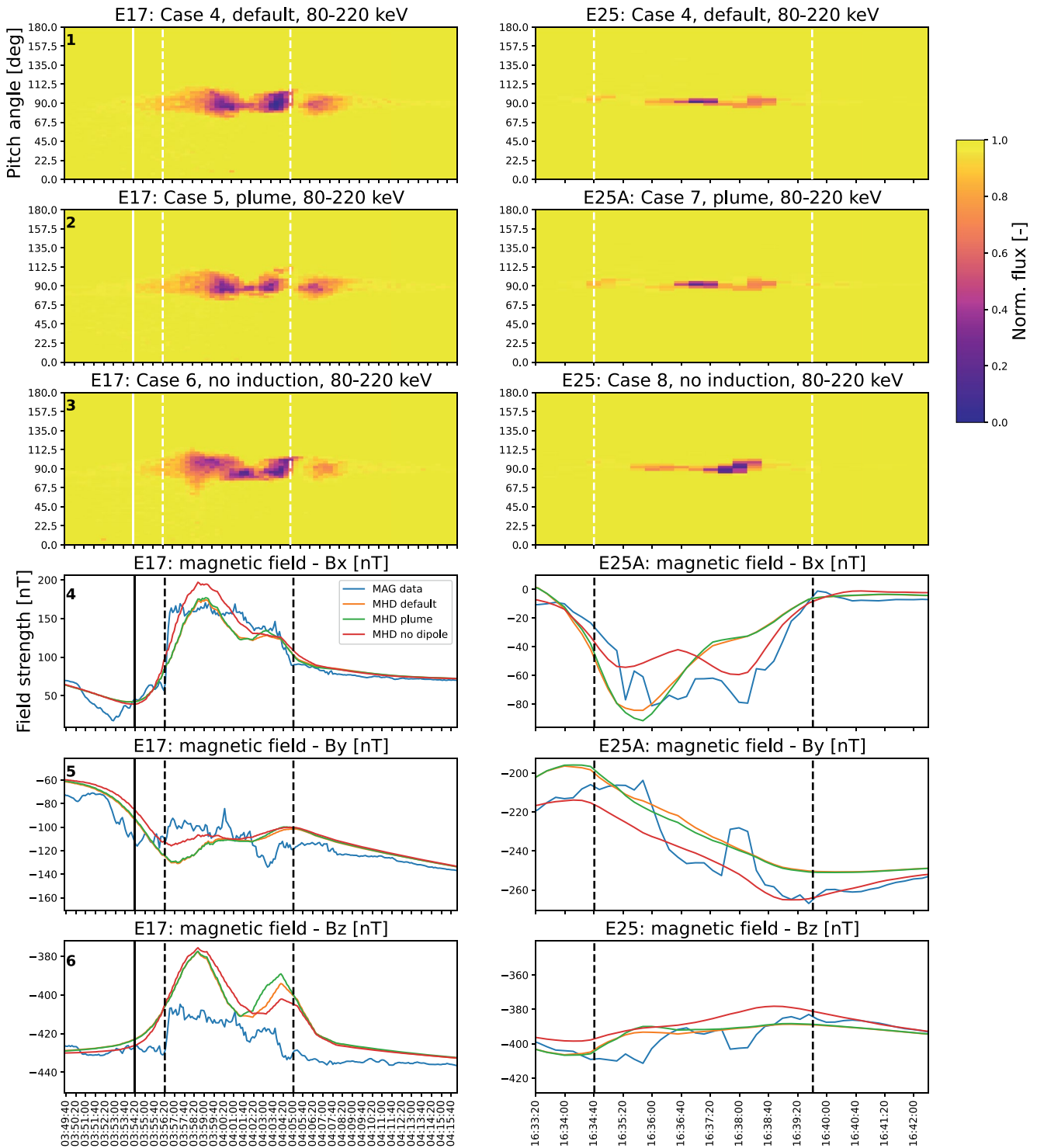
Figure 12. Comparison of simulations for the TP1 channel 80–220 keV protons (Panel 1–3), magnetic field data and MHD simulations (Panel 4–6). The left column represents flyby E17 and the right column flyby E25A. The solid vertical line indicates the closest approach. The dashed vertical lines indicate the time of the encounter with the Alfvén wing, as discussed in Appendix D.

the presence of an induced dipole. Differences between the simulated and real fields are thus a plausible cause of the discrepancy.

We emphasize that the simulated electromagnetic fields are only constrained by magnetic field measurements taken along the spacecraft trajectory, whereas the energetic protons traverse large sections of the perturbed field, and are thus also sensitive to perturbations that cannot be known from the along-the-flight-path field measurements. This implies that in the absence of more magnetic field measurements the energetic proton measurements can thus provide additional constraints on the structure of the electromagnetic fields near Europa. Simulating magnetic field data along the trajectory alone is a good first step, but ideally ions sensitive to global aspects of the interaction region's structure should also be reconstructed well to gain confidence that any derivative interpretation from the simulated MAG data (in the context of oceans, plumes, exosphere, interaction physics) is valid.

Next we discuss possible causes for the discrepancy between the MHD simulations and the magnetic field data. For E17 we observe that the Bx component is reproduced relatively well, but the perturbation in the Bz component is overestimated, as can be seen in Figure 12. In the MHD results of (Blöcker et al., 2016), who apply a radially symmetric atmosphere, the discrepancy between the modeled and the measured Bz component is a bit smaller, but the magnitude is still overestimated. Thus one possible explanation is that the asymmetric atmosphere during E17 is not properly described by the model. Besides the atmospheric effects, it is possible that other effects play a role in the modification of the magnetic field which are not included in our MHD model such as sudden magnetospheric effects (e.g., flux tube interchange).

We cannot fully exclude missing physics either, studies of moon-magnetosphere interaction at different objects have indeed shown that discrepancies in the magnetic field model can be a sign of missing physics, for example, Kriegel et al. (2011) revealed the importance of dust in Enceladus' plume from a discrepancy in just one component of the magnetic field, which illustrates the sensitivity of such modeling efforts. While our MHD model for E17 produces perturbations in the field magnitude that are on the order of those observed, the MHD model does not predict any perturbations in the field magnitude during E25A, even though small perturbations (on the order of 10 nT) occur in the measurements (see Figure 3 in Volwerk et al., 2007) suggesting that indeed some physical effects could be missing, potentially of a kinetic or turbulent nature. We consider it out of the scope of the current study to identify the precise cause of these magnitude perturbations.

For E25A the comparison between the MAG and the MHD data in Figure 12 shows that the MHD model does not capture the whole width of the wing, especially at the exit point, visible in the B_x component. Indeed, after the wing exit is where we observe a discrepancy between the simulated proton flux and the proton measurements. As described above, we do not produce a proton depletion in our model after the wing exit, while one occurs in the measurement. This strongly suggests that the fields play a role in the discrepancy between the simulated and measured dropout. A possible cause of the difference between the simulated and measured magnetic field is the resolution of the MHD simulation. Due to the lower resolution, as well as the finite resistivity and viscosity in the MHD code, the Alfvén wing structures in the electromagnetic fields are more smeared out further away from the moon (at the E25A trajectory). Furthermore, the discrepancy could also be attributed to a slightly different bending of the northern wing in the simulation compared to the measured wing from the MAG data. As shown in Figure D2 a small shift of the trajectory would lead to slightly different signal in the magnetic field. The bending of the wing depends on different plasma parameters, such as the background magnetic field, the upstream plasma velocity, the density, and the induced field from a subsurface ocean. Furthermore, the MAG data contains small scale perturbations inside the Alfvén wing (see e.g., the By component in Figure 12) which are not captured by the MHD model. These small scale perturbations could be due to a localized inhomogeneity in the atmosphere or some small-scale dynamic plasma processes (see Blöcker et al., 2016).

There are several independent MHD models trying to reproduce the Galileo data Schilling et al. (2007); Blöcker et al. (2016); Arnold et al. (2019); Harris et al. (2021); Cervantes and Saur (2022). However, none of them have a perfect fit to all the flybys. It might be that we have to adjust the atmospheric model to every flyby, meaning that Europa's atmosphere is not stable with time. Furthermore, as mentioned in Blöcker et al. (2016) we might miss some effects by interpreting only the magnetic field data for the plasma interaction. We require both the velocity and magnetic field measurements to separate between a pure Alfvénic structure such as generated by an asymmetry in the atmosphere/plume and magnetospheric structures which convect across Europa and its Alfvén wings. Convecting magnetospheric signatures might simply be pressure-balanced structures which do not obey the Alfvénic relationship between the magnetic field perturbation and the velocity field perturbation.

Further discrepancies between the simulated and real electromagnetic field could arise due to differences in the upstream conditions (density, velocity) of the corotating plasma from the values in the simulation. The MHD simulation results strongly depend on the upstream plasma conditions used in the model. Previously it has been demonstrated that the angle of the Alfvén wing with respect to the ambient magnetic field increases as a function of the ambient plasma density (Harris et al., 2021; Neubauer, 1980). Thus, discrepancies between the initial conditions (shown in Table 4) and the real magnetospheric conditions could affect the perturbed electromagnetic fields and thereby contribute to the discrepancies between the proton measurement and the simulation results. We recommend that future studies investigate the sensitivity of the proton losses to upstream magnetospheric conditions.

Next we compare the proton simulations to the magnetic field simulations and magnetic field data. In Figure 1 it was already shown that the measured magnetic field perturbation associated with the Alfvén wing coincides with the measured energetic proton depletions. An overview with line plots of the proton simulations, MHD simulations and magnetic field data are shown in Figure 12. We observe that both the simulated depletion in E17 and the simulated Bz magnetic field component in the MHD simulations have a double lobed structure: in the simulated flux for E17 there are two distinct local maxima of the depletion (panel 1 and 2) and in the simulated Bz component there are two local maxima. While for E25A there is no such double lobe in the simulated Bz component nor the simulated depletion. This suggest that it could be the double lobed structure in the simulated magnetic field that shapes the double maxima of depletion in the proton simulation during E17. Thus a better fit for the simulated Bz component to the measured Bz could also improve the fit of the proton simulation. To determine the sensitivity of the measured proton depletions to these type of double lobed structures in the field would require a wider investigation of the parameter space which is outside of the scope of this paper.

Other discrepancies could occur due to differences in the upstream distribution of the energetic protons. Here only one profile was assumed. Further studies could investigate the sensitivity of the energetic proton energy distribution on the depletion in the Alfvén wings.

Finally, discrepancies between the simulated and real fields also occur due to the technical limitations of the simulations. Specifically, the resolution of the MHD simulation becomes larger further away from Europa (see Section 5): up to 450 km in radial direction for E17 and 320 km for E25A. The resolution could thus become larger than the gyroradius of the particle involved (see Figure B1), meaning that the particles will not experience some of the gradients that could exist in reality and might therefore not be deflected. In this sense our simulation could underestimate the effect of the perturbed fields. This could explain why the depth of the depletion is underestimated in our simulation.

We have identified various physical effects and limitations of the simulation that could contribute to the discrepancy between the proton simulation and the proton measurement. However, due to the poor spatial and temporal resolution of the data we consider it unlikely that a definitive interpretation of the measurement can be reached.

We conclude that even though differences between data and simulation remain, at least qualitatively, the inhomogeneous simulations show a better agreement with the data. We recommend that future studies investigate the wider parameter space using high resolution simulations of the perturbed fields to identify a field configuration that provides a better fit to the EPD data.

6.6. Implications for Future Measurements and Missions

Our results show that energetic proton depletions can be detected in Europa's Alfvén wings. The pitch angle distribution and depth of the depletions can be modified by perturbed fields associated with the Alfvén wings, ionosphere, the induced dipole and potentially plumes. While even in low resolution data, such as the EPD data considered in this work, the effect of the field perturbation associated with Alfvén wing can be seen in the data, high pitch angle and time resolution data could also reveal contributions by Europa's induced dipole or perhaps plumes. This indicates that energetic proton measurements can also be used to probe Europa's magnetospheric interaction, during flybys that are not close to the surface. The added value of the energetic protons is that they traverse the whole environment in a short amount of time and therefore contain information on the larger structure of the environment, while the magnetic field data only provides a measurement along the trajectory. Thus we emphasize the importance of high resolution measurements (in time, direction and

energy) of energetic ions close and in the Alfvén wings, to complement the magnetic field and plasma measurements. Future high resolution measurements could reveal detailed aspects of the Alfvén wing and related field configuration.

Our finding on the importance of energetic proton measurements during remote flybys applies in general to future mission to moons of outer planets with Alfvén wings and energetic particle populations, where data might be gathered only during a very limited number of flybys. For example, at the moons of the ice giants, such as Triton. Liuzzo et al. (2021) have modeled different Alfvén wing configurations at Triton, demonstrating that the Alfvén wings can both reside downstream of the plasma flow, but also a configuration is possible with one wing upstream of the moon and the other downstream. Trident has been proposed as a single encounter mission to explore Triton (Frazier et al., 2020). Having energetic ion measurements available during such encounters of data-starved objects, in addition to magnetic field data, will allow to better constrain the moon-magnetosphere interaction and potentially find signatures of subsurface oceans.

An energetic ion detector that provides a higher time resolution than Galileo's EPD and information about the particle's pitch angle, could be able to distinguish these induced dipole or dense plume features. The effect of the induced dipole on the proton depletions will be maximum when Europa is encountered at large magnetic latitudes. One mission with the desired capability is the JUpiter ICy moon Explorer (JUICE) (Grasset et al., 2013) which is equipped with the instrumentation to detect energetic protons (Barabash et al., 2016). However, JUICE currently has only two Europa flybys planned, with a closest approach at 400 km. No dedicated Alfvén wing passes have been planned yet. Another mission of interest is the current Juno mission which will encounter Europa during its extended mission and is equipped with the energetic ion detector JEDI (Mauk et al., 2017).

7. Conclusion

We identify energetic proton depletions (88–540 keV) during the distant E17 and E25A Galileo flybys of Europa, which both encounter Europa's Alfvén wings. We simulate the proton trajectories near Europa and find that inhomogeneous electromagnetic fields associated with the Alfvén wings and ionosphere strongly modify the pitch angle distribution and depth of the depletion. Whereas the homogeneous case gives a depletion that is very narrow in pitch angle without structure, the inhomogeneous case results in complex structure of the depletion in terms of pitch angle dependence. Thus, the field perturbations are strong enough to have an impact not just on the energetic ion distributions reaching the surface, but also on the moon's external environment, at least several Europa radii away from the moon. Furthermore we show that the induced dipole modifies the pitch angle distribution of the proton losses and in the case of E25A shifts the maximum of depletion along the trajectory.

The plumes considered in this study have a minor effect on the proton depletions along the Alfvén wings, compared to the contribution of the perturbed fields associated with the Alfvén wings and ionosphere. It appears unlikely that a plume with a density of 2.5×10^{15} m^{-3} could be identified solely based on the measured proton dropouts during E17 and E25A.

We find that a model in which the electromagnetic fields around Europa are not perturbed, and wherein the Alfvén wings or perturbations associated with the ionosphere do not exist, are not able to reproduce the measured proton depletion (88–540 keV). On the other hand, the model with the perturbed fields and Alfvén wings agrees qualitatively better with the measurement. Thereby suggesting that the field perturbations are indeed responsible for the measured proton dropouts.

We attribute the remaining discrepancies between the simulated proton dropouts and the measurements to discrepancies between the simulated and real electromagnetic fields. We argue that simulating the electromagnetic fields along the trajectory is a good first step, but that ideally the energetic ion flux is reconstructed well to gain confidence in the interpretation of the simulated magnetic field.

This study emphasizes that energetic proton measurements could offer an additional way to probe the (sub-Alfvénic) moon-magnetosphere interaction from large distances of several moon radii away, not only at Europa but also at other objects. Instruments with a better spatial and temporal resolution than Galileo's Energetic Particle Detector could study the complex interaction of the energetic ions with Europa's Alfvén wings, which is also influenced by Europa's dipole and potential plumes.

Appendix A: Charge Exchange Cross Section

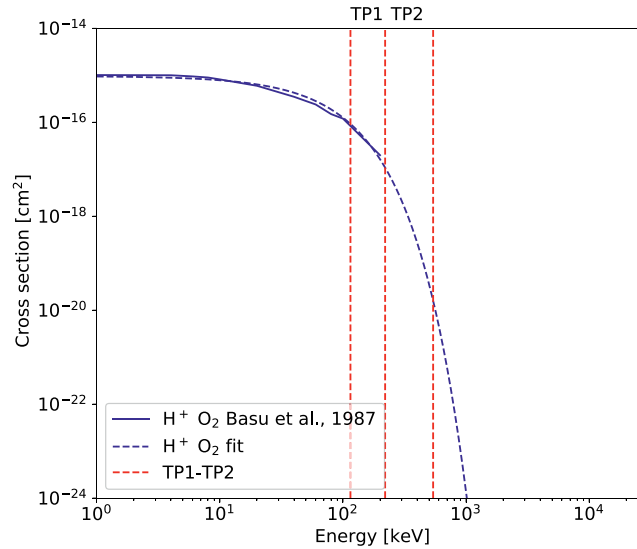The charge exchange cross section of H^+ with O_2 as used in the simulations is shown in Figure A1.

Figure A1. Charge exchange cross section of H^+ with O_2 from Basu et al. (1987) (solid blue line) and a fit to the spectrum (dashed blue line). The red dashed vertical lines indicate the energy range of the TP channels. The first and second dashed red lines indicate the energy range of the TP1 channel (80–2,220 keV). The second and third dashed red lines indicate the range of the TP2 channel (220–540 keV). The energy range is based on the calibration values from Williams et al. (1992).

Appendix B: Proton Gyroradius

The proton gyroradius for different pitch angles and the energy range considered in the simulations and data is shown in Figure B1.
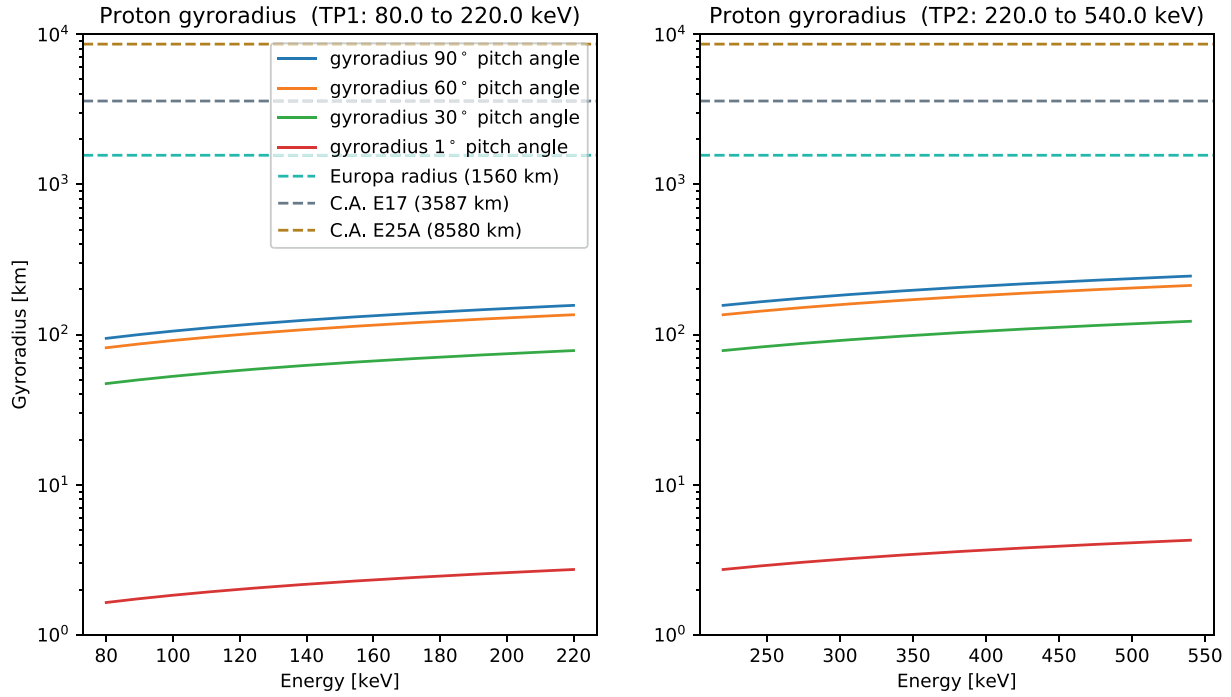

Figure B1. Gyroradius for different pitch angles over the energy range of the TP1 channel (left) and TP2 (right). The magnetic field is the background field assumed in the simulation (see Table 4). Also indicated are several scales of interest: the radius of Europa and the altitude of the closest approach.

Appendix C: Proton Bounce Period

The proton bounce period for different pitch angles and the energy range considered in the simulations and data is shown in Figure C1.
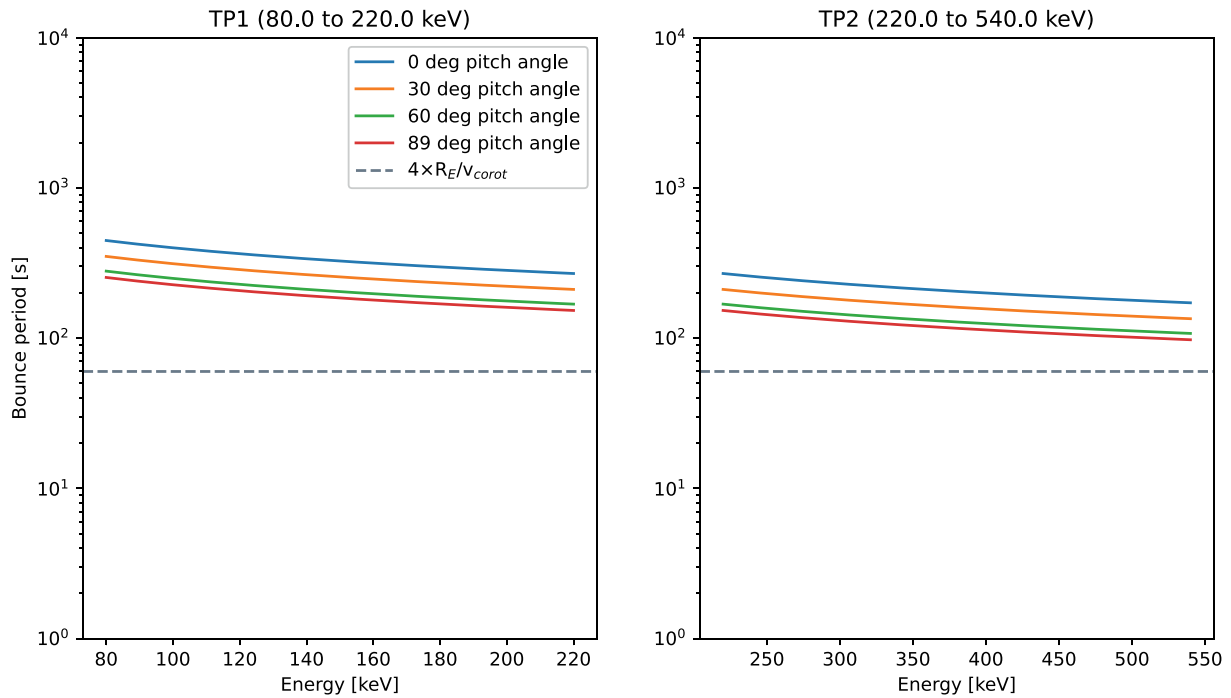

Figure C1. Bounce period for different pitch angles over the energy range of the TP1 channel (left) and TP2 (right). Also indicated by the dashed gray line is the bounce period required for a particle to impact Europa and re-enter the simulation box at 4 R_E. The Alfvén wings are encountered within $4R_E$. The bounce period of the particles considered is above the gray line, we therefore consider that particles that have encountered Europa in the simulation need not to re-enter the simulation box near the Alfvén wing. The bounce period is calculated using Equation 2.2 from Baumjohann and Treumann (1997). The co-rotational speed is the speed assumed in the MHD simulation (see Table 4).

Appendix D: MHD Simulations

The magnetic field perturbations during E17 simulated for cases 3–4 (without plume) and 5 (with plume) are shown in Figure D1. The plume especially affects the Bx and Bz component in the center of the Alfvén wing but has not much influence at the edge of the Alfvén wing where Galileo encounters the northern wing. In the upper panels of Figure D2 we show the trajectory of Galileo and the magnetic field environment from an MHD simulation (cases 3–4) during the E17 flyby. Galileo crossed downstream the edge of the southern Alfvén wing which is especially visible in the perturbed B_x component. The magnetic field experiences a strong perturbation in the positive x direction due to the bending of the magnetic field lines south of Europa. This perturbation of B_x has an elliptical shape since we show a crosssection at constant z through a bended cylinder. The crosssection is shifted to the positive x direction because of the plasma flow and slightly shifted to the negative y direction because of the background magnetic field during E17 (see Table 4). The comparison between the measured MAG data during E17 and the MHD simulation results, presented in Figure 12 panels 4–6, show that the MHD results fit the overall structure of B_x and B_y very well. B_z is overestimated by our MHD model. The cyan and magenta dots in Figure D2 represent the location of the entry/exit of Galileo into/out of the area influenced by the Alfvén wings. We chose the entry point at the beginning of the steep increase (decrease) of B_x and the exit at the end of the steep decrease (increase) of B_x for the southern (northern) wing. The entry and exit times for E17 are 03:56:16 UTC and 04:04:58 UTC, and for E25 are 16:34:00 UTC and 16:39:48 UTC. They are shown by the dashed lines in Figure 12. During E25A Galileo passed downstream of the northern Alfvén wing toward Jupiter. The flyby occurred farther away from Europa and therefore has a lower resolution in both, MAG data and MHD results. The crosssection of the northern Alfvén wing is recognizable in the decrease of the B_x component. The crosssection of the northern Alfvén wing is not only shifted in the positive x direction but also in the

positive y direction due to the strong negative B_y component of the background magnetic field (see Figure D2). The comparison between the MAG and the MHD data in Figure 12 shows that the MHD model does not capture the whole width of the wing, especially at the exit point, visible in the B_x component probably due to the coarse resolution of the MHD results.
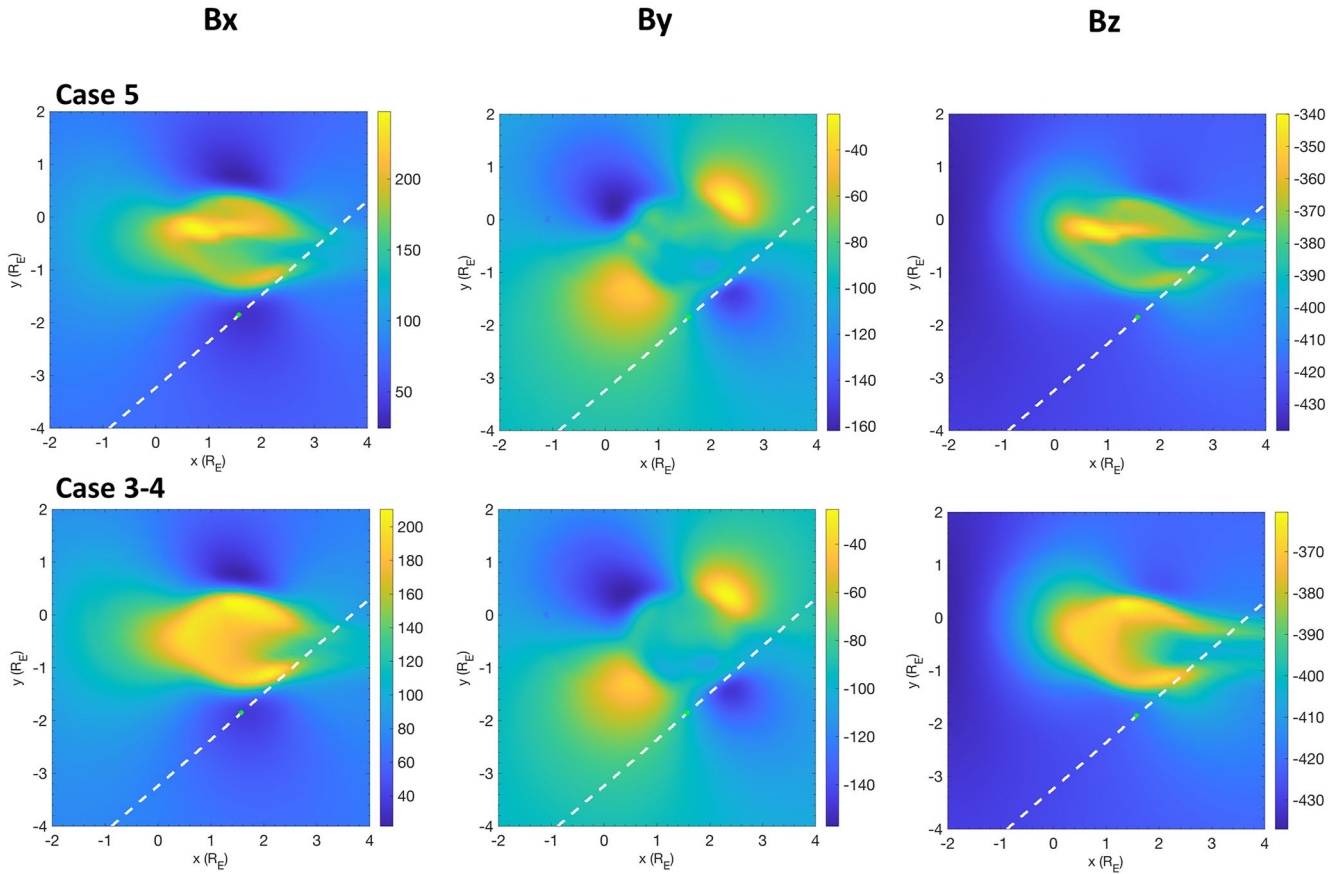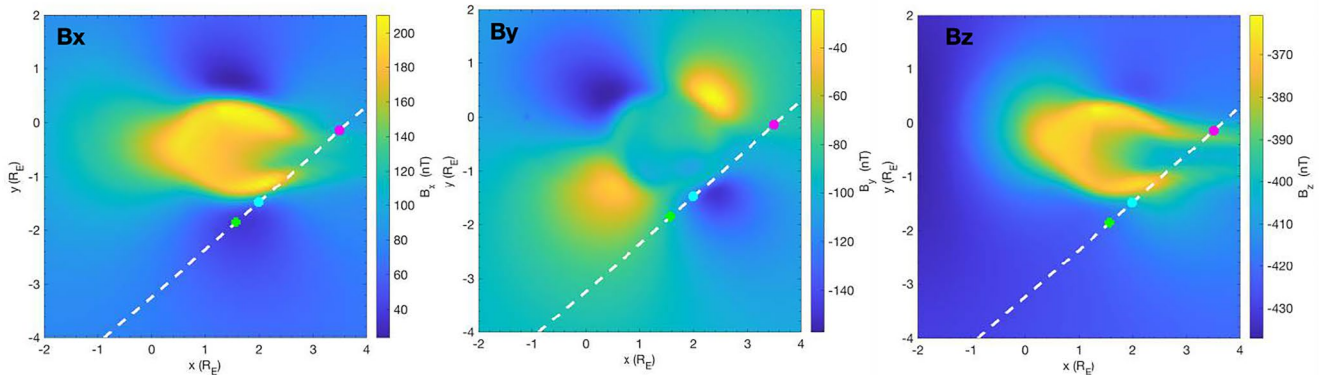

Figure D1. E17 MHD simulations for Case 5 (with plume) and Cases 3–4 (no plume). The figures represent the magnetic field components in nT in an X-Y cut through the Alfvén wing, south of Europa at $z = -2.23\ R_E$. The dashed line represents the flyby trajectory.
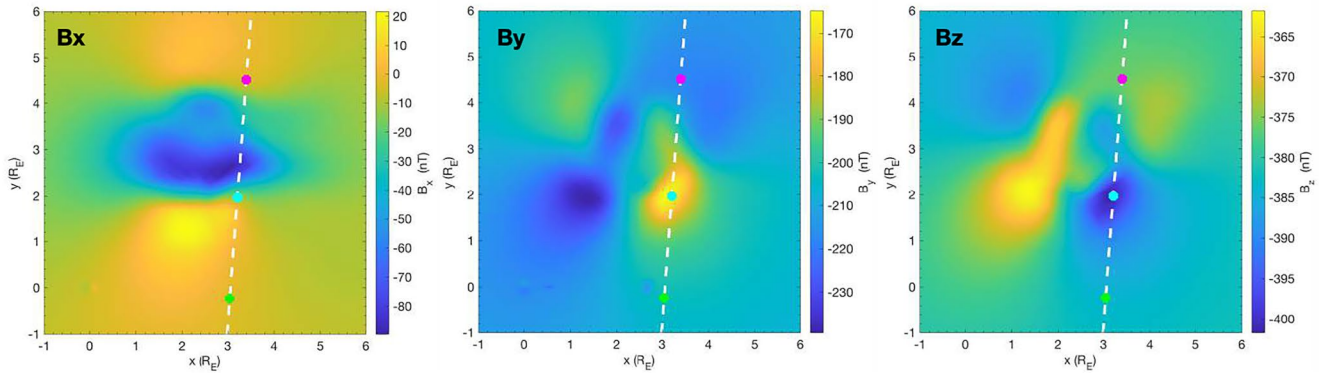
E17: Cases 3-4

E25: Cases 3-4

Figure D2. E17 and E25 MHD simulations for cases 3–4 (no plume). The figures represent the magnetic field components in nT in an X-Y cut through the Alfvén wing, south of Europa at $z = -2.23\ R_E$ (E17) and north of Europa at $z = 5.79\ R_E$ (E25). The dashed lines represent the flyby trajectories. The green dots display the location of the closest approach at 03:53:52 UTC (E17) and 16:29:00 UTC (E25). The cyan and magenta dots represent the entry/exit of Galileo into/out of the area mainly perturbed by the Alfvén wings according to the MAG data.

Although the MHD simulation results shown here are produced with the atmospheric model described in Section 4, the results are very similar to those from the MHD model with a radially symmetric atmosphere presented by Blöcker et al. (2016).

Appendix E: Reconstruction of the EPD Pointing

For a comparison of the simulation with the EPD data a reconstruction of the EPD pointing is required. A major challenge specific to this study is that only the low resolution LGA data product is available for E17 and E25A, whereas in our previous study Huybrighs et al. (2020) the high resolution data product HGA was available for flyby E26.

It is our understanding that the specific details on the operation principle of EPD, pertaining to the data segments of flybys E17 and E25A presented in this work, were not previously published. Some, but not all, aspects relevant to the EPD LGA data are documented in Lagg (1998) and Jaskulek (1999). The information presented in this section is based on personal correspondence with Steve Jaskulek and Andreas Lagg. Our findings on the LGA mode will also be documented in the EPD user manual (Kollmann et al., 2022).

In the LGA mode the data are stored in 16 sectors that together represent the sky, as opposed to the high resolution mode (HGA) wherein data are stored in the sequence they are measured in. Thus, the timetags assigned to the 16 sectors in the LGA mode are artificial, only the start and end time of each series of measurements lasting 228

(E17) or 342 (E25A) seconds is known. Note that almost the full sky is scanned, as the EPD motor positions from 1 to 6 are scanned during this mode.

Furthermore, during the LGA mode in E17 the sectors are averaged over two instrument cycles, and over three in E25A. During each cycle the sky is scanned once, or practically speaking one skymap is generated. If the data from a single cycle or skymap were preserved, we could reconstruct when a measurement was taken. However, effectively the measurements in the sectors of two or three skymaps are averaged together while the original skymaps were not transmitted to Earth. Thereby the information of the sector in which a measurement was made is retained, but the information about when a measurement was taken (within the two or three cycles) is lost. Together the two cycles last 228 s (E17) and 342 s (E25A). In conclusion, it cannot be be determined if a measurement was obtained during the first or the second cycle, thus resulting in a maximum uncertainty of 228 s (E17) or 342 s (E25A) of the time of the measurement.

The two panels in Figure E1 visualize the two sky maps that are combined to form one 'list' of 16 data points (or sectors), see Table E1 during flyby E17. In each sky map the horizontal axis represents the spin direction and the vertical axis the motor direction. EPD-CMS can make a full scan of the sky by moving the CMS telescope over 7 motor positions, changing motor position once every spin. The arrows next to the axis represent the direction in which the spin and the motor positions are scanned. The numbers represent the order in which the measurements are taken. Note that motor position 0 corresponds to a position where the instrument is behind the calibration shield, these measurements are not incorporated in the data product. Motor position 7, which has shown to be affected by an artifact that creates nonphysical dropouts (Jia et al., 2021; Huybrighs et al., 2021), is not included in this mode.
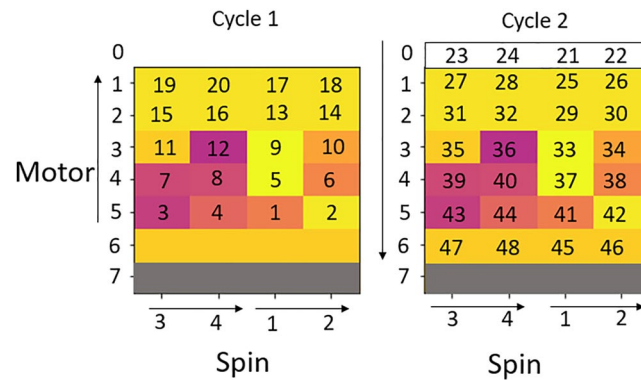

Figure E1. During E17 two scans of the sky (cycle 1 and 2), or equivalently two skymaps, are combined into a series of 16 data points, corresponding to the 16 sectors of the sky. The colors represent data as shown in the middle panel of Figure 2. The horizontal axis of each panel represents the directions scanned resulting from the spin of the spacecraft, the vertical axis represent the directions scanned by moving the motor position. The numbers in each element represent the order in which measurements are taken, these numbers are used in Table E1 to explain how the 16 data values are obtained.

Table E1
The First Column Represents the 16 Data Values or Sectors in Each Data List That Result From Combining the Elements of Two Cycles (or Two Skymaps) in Figure E1 Into a New Averaged Skymap. The Numbers in the Right Column Refer to the Elements in Figure E1 That Are Averaged Together

Line in data list	Corresponding values in Figure E1
1st line	13,14,17,18 and 29,30,25,26
2nd line	15,16,19,29 and 31,32,27,28
3rd line	9 and 33
4th line	5 and 37

Table E1
Continued

Line in data list	Corresponding values in Figure E1
5th line	1 and 41
6th line	10 and 34
7th line	6 and 38
8th line	2 and 42
9th line	11 and 35
10th line	7 and 39
11th line	3 and 43
12th line	12 and 36
13th line	8 and 40
14th line	4 and 44
15th line	45 and 46
16th line	47 and 48

Table E1 shows how each of the lines of the 16-line data (or sector) list corresponds to the elements of the two cycles. The 16 sector values are combined by averaging over the number of measurements and elements that are combined from the initial two skymaps. This table applies specifically to flyby E17.

Like in Huybrighs et al. (2020) the pointing of EPD was obtained using a dedicated software package originally developed by Andrew Poppe. This software requires two main inputs: the motor position corresponding to each measurement and the rotor files (https://doi.org/10.17189/1519675).

The motor positions during the LGA mode are not explicitly stored, as for the HGA data. However, the motor numbers can be reconstructed as follows. Please note that while we can reconstruct the motor sequence, it does not mean that we can reconstruct the order of the measurements due to the averaging of cycles (or equivalently skymaps) as discussed in the previous paragraphs. The LGA data is divided in lists of 16 values that represent the 16 sectors which correspond to the two scans of the sky. For each list of 16 data points the initial motor position is known. Then, using the information of how the motor number evolves one can reconstruct the order in which the motor numbers occurred. The initial motor positions is obtained from the "subcom" field in the "epd-header block." The epd-header block is exported by the EPD software package by Andreas Lagg. An example of a line of this block looks like this, for flyby E17:

```
TFDOS: 1998.269032205 TLDOS: 1998.269032553 0 74 179 1 22 30
```

The last number, 30, or 0001 1110 in binary, is key here. The value of the fourth bit, 1, indicates that the direction of rotation of the motor is clockwise (CW). The last 3 bits can be read as 110 binary, or 6 decimal. Meaning that the last motor position of the data block is 6. Combining this value with the clockwise rotation direction implies that the initial motor position of the next block is 5. Following the CW to get to 6 the following positions have to be cycled through $1 \rightarrow 2 \rightarrow 3 \rightarrow 4 \rightarrow 5 \rightarrow 6$. The next step, and therefore the beginning of the science record, should thus be position 5, followed by $4 \rightarrow 3 \rightarrow 2 \rightarrow 1 \rightarrow 0$. The value 30 is the same for all data blocks considered, and therefore the starting motor position is the same for each block. This is consistent with the time tagging of the data. The time of each record appears to be 228 s, which is twice the motor cycle time of 114 s, so each record is 2 motor cycles (there and back). Given this even number of motor cycles, the motor position should always finish where it started (i.e., $5 \rightarrow 4 \rightarrow 3 \rightarrow 2 \rightarrow 1 \rightarrow 0 \rightarrow 1 \rightarrow 2 \rightarrow 3 \rightarrow 4 \rightarrow 5 \rightarrow 6$, then repeating with $5 \rightarrow 4 \rightarrow 3 \rightarrow 2 \rightarrow 1 \rightarrow 0 \rightarrow 1 \rightarrow 2 \rightarrow 3 \rightarrow 4 \rightarrow 5 \rightarrow 6$ and so on).

For flyby E25 the situation is more complicated. First, the 16 sectors are averaged over three instrument cycles instead of two. Second, the order of the EPD motor positions is not the same for every skymap composed of three instrument cycles. This is implied by the following two lines from the subcom field. The last number

(which indicates the motor direction) alternates between 29 and 9 for subsequent sky maps averaged over 342 s. The difference in number implies that the last motor number is different.

```
TFDOS: 1999.329160701 TLDOS: 1999.329161242 0 78 225 1 13 29
TFDOS: 1999.329161243 TLDOS: 1999.329161825 0 79 185 1 0 9
```

Therefore, the motor numbers for the first line of the subcom field will be:

$$0 \rightarrow 1 \rightarrow 2 \rightarrow 3 \rightarrow 4 \rightarrow 5 \rightarrow 6 \rightarrow 5 \rightarrow 4 \rightarrow 3 \rightarrow 2 \rightarrow 1 \rightarrow 0 \rightarrow 1 \rightarrow 2 \rightarrow 3 \rightarrow 4 \rightarrow 5$$

While the motor numbers for the second line will be:

$$\rightarrow 6 \rightarrow 5 \rightarrow 4 \rightarrow 3 \rightarrow 2 \rightarrow 1 \rightarrow 0 \rightarrow 1 \rightarrow 2 \rightarrow 3 \rightarrow 4 \rightarrow 5 \rightarrow 6 \rightarrow 5 \rightarrow 4 \rightarrow 3 \rightarrow 2 \rightarrow 1$$

After this the pattern will repeat again.

$$\rightarrow 0 \rightarrow 1 \rightarrow 2 \rightarrow 3 \rightarrow 4 \rightarrow 5 \rightarrow 6 \rightarrow 5 \rightarrow 4 \rightarrow 3 \rightarrow 2 \rightarrow 1 \rightarrow 0 \rightarrow 1 \rightarrow 2 \rightarrow 3 \rightarrow 4 \rightarrow 5 \rightarrow 6 \rightarrow 5 \rightarrow$$

Thus, to express the sequence of motor numbers for each 342 s cycle two different tables, equivalent to E1, would have to be formulated (one for lines with the last subcom field 29 and a different one for those with the last subcom field value 9). As well as two sets of three panels each equivalent to Figure E1.

Besides the motor number also the rotor files are required. Around the Alfvén wing encounter the rotor file has no data (E17) or the resolution is limited to two data points (E25A). We attempted to reconstruct the rotor file by assuming the right ascension "ra" and declination "dec" angle remain constant over the Alfvén wing encounter compared to the data points available within several minutes after the encounter. Second we assume the variation of the twist and spin angle repeats itself compared to the data points available after the Alfvén wing encounter. The AACS files for the MAG instrument retain similar gaps as for the rotor files and therefore provide no better source of the rotor angles.

Data Availability Statement

Galileo EPD data are available through NASA's Planetary Data System (PDS) (PDS, 2022). Simulations are available online in Huybrighs et al. (2023).

References

Addison, P., Liuzzo, L., Arnold, H., & Simon, S. (2021). Influence of Europa's time-varying electromagnetic environment on magnetospheric ion precipitation and surface weathering. *Journal of Geophysical Research: Space Physics*, *126*(5), e2020JA029087. https://doi.org/10.1029/2020JA029087

Addison, P., Liuzzo, L., & Simon, S. (2022). Effect of the magnetospheric plasma interaction and solar illumination on ion sputtering of Europa's surface ice. *Journal of Geophysical Research: Space Physics*, *127*(2), e2021JA030136. https://doi.org/10.1029/2021JA030136

Arnold, H., Liuzzo, L., & Simon, S. (2019). Magnetic signatures of a plume at Europa during the Galileo E26 flyby. *Geophysical Research Letters*, *46*(3), 1149–1157. https://doi.org/10.1029/2018GL081544

Barabash, S., Brandt, P. C., & Wurz, P., & the PEP team. (2016). *Particle environment package (PEP) for the ESA juice mission*. American Astronomical Society. DPS meeting # 48.

Basu, B., Jasperse, J. R., Robinson, R. M., Vondrak, R. R., & Evans, D. S. (1987). Linear transport theory of auroral proton precipitation: A comparison with observations. *Journal of Geophysical Research*, *92*(A6), 5920–5932. https://doi.org/10.1029/JA092iA06p05920

Baumjohann, W., & Treumann, R. (1997). *Basic space plasma physics*. Imperial College Press.

Birdsall, C. K. (1991). Particle-in-cell charged-particle simulations, plus Monte Carlo collisions with neutral atoms, PIC-MCC. *IEEE Transactions on Plasma Science*, *19*(2), 65–85. https://doi.org/10.1109/27.106800

Blöcker, A., Roth, L., Ivchenko, N., & Hue, V. (2020). Variability of Io's poynting flux: A parameter study using MHD simulations. *Planetary and Space Science*, *192*, 105058. https://doi.org/10.1016/j.pss.2020.105058

Blöcker, A., Saur, J., & Roth, L. (2016). Europa's plasma interaction with an inhomogeneous atmosphere: Development of Alfvén winglets within the Alfvén wings. *Journal of Geophysical Research: Space Physics*, *121*(10), 9794–9828. https://doi.org/10.1002/2016ja022479

Blöcker, A., Saur, J., Roth, L., & Strobel, D. F. (2018). MHD modeling of the plasma interaction with Io's asymmetric atmosphere. *Journal of Geophysical Research: Space Physics*, *123*(11), 9286–9311. https://doi.org/10.1029/2018JA025747

Breer, B. R., Liuzzo, L., Arnold, H., Andersson, P. N., & Simon, S. (2019). Energetic ion dynamics in the perturbed electromagnetic fields near Europa. *Journal of Geophysical Research: Space Physics*, *124*(9), 7592–7613. https://doi.org/10.1029/2019JA027147

Carnielli, G., Galand, M., Leblanc, F., Leclercq, L., Modolo, R., Beth, A., et al. (2019). First 3D test particle model of Ganymede's ionosphere. *Icarus*, *330*, 42–59. https://doi.org/10.1016/j.icarus.2019.04.016

Carnielli, G., Galand, M., Leblanc, F., Modolo, R., Beth, A., & Jia, X. (2020a). Constraining Ganymede's neutral and plasma environments through simulations of its ionosphere and Galileo observations. *Icarus*, *343*, 113691. https://doi.org/10.1016/j.icarus.2020.113691

Carnielli, G., Galand, M., Leblanc, F., Modolo, R., Beth, A., & Jia, X. (2020b). Simulations of ion sputtering at Ganymede. *Icarus*, *351*, 113918. https://doi.org/10.1016/j.icarus.2020.113918

Cassidy, T., Paranicas, C., Shirley, J. D. III, Teolis, B., Johnson, R., Kamp, L., et al. (2013). Magnetospheric ion sputtering and water ice grain size at Europa. *Planetary and Space Science*, *77*, 64–73. https://doi.org/10.1016/j.pss.2012.07.008

Cervantes, S., & Saur, J. (2022). Constraining Europa's subsolar atmosphere with a joint analysis of HST spectral images and Galileo magnetic field data. *Journal of Geophysical Research: Space Physics*, *127*(9), e2022JA030472. https://doi.org/10.1029/2022JA030472

Clark, G., Mauk, B. H., Paranicas, C., Kollmann, P., & Smith, H. T. (2016). Charge states of energetic oxygen and sulfur ions in Jupiter's magnetosphere. *Journal of Geophysical Research: Space Physics*, *121*(3), 2264–2273. https://doi.org/10.1002/2015JA022257

Curry, S. M., Liemohn, M., Fang, X., Ma, Y., Slavin, J., Espley, J., et al. (2014). Test particle comparison of heavy atomic and molecular ion distributions at Mars. *Journal of Geophysical Research: Space Physics*, *119*(3), 2328–2344. https://doi.org/10.1002/2013JA019221

De La Fuente Marcos, R., & Nissar, A. (2000). Possible detection of volcanic activity on Europa: Analysis of an optical transient event. *Earth, Moon, and Planets*, *88*(3), 167–175. https://doi.org/10.1023/A:1016561713096

Duling, S., Saur, J., & Wicht, J. (2014). Consistent boundary conditions at nonconducting surfaces of planetary bodies: Applications in a new Ganymede MHD model. *Journal of Geophysical Research: Space Physics*, *119*(6), 4412–4440. https://doi.org/10.1002/2013JA019554

Frazier, W., Bearden, D., Mitchell, K. L., Lam, T., Prockter, L., & Dissly, R. (2020). Trident: The path to triton on a discovery budget. In *2020 IEEE aerospace conference* (pp. 1–12). https://doi.org/10.1109/AERO47225.2020.9172502

Futaana, Y., Barabash, S., Holmstrom, M., Fedorov, A., Nilsson, H., Lundin, R., et al. (2010). Backscattered solar wind protons by phobos. *Journal of Geophysical Research*, *115*(A10). https://doi.org/10.1029/2010ja015486

Futaana, Y., Machida, S., Saito, Y., Matsuoka, A., & Hayakawa, H. (2003). Moon-related nonthermal ions observed by nozomi: Species, sources, and generation mechanisms. *Journal of Geophysical Research*, *108*(A1), 1025. https://doi.org/10.1029/2002ja009366

Grasset, O., Dougherty, M., Coustenis, A., Bunce, E., Erd, C., Titov, D., et al. (2013). Jupiter icy moons explorer (juice): An ESA mission to orbit Ganymede and to characterise the Jupiter system. *Planetary and Space Science*, *78*, 1–21. https://doi.org/10.1016/j.pss.2012.12.002

Harris, C. D. K., Jia, X., Slavin, J. A., Toth, G., Huang, Z., & Rubin, M. (2021). Multi-fluid MHD simulations of Europa's plasma interaction under different magnetospheric conditions. *Journal of Geophysical Research: Space Physics*, *126*(5), e2020JA028888. https://doi.org/10.1029/2020JA028888

Hayes, J. C., Norman, M. L., Fiedler, R. A., Bordner, J. O., Li, P. S., Clark, S. E., et al. (2006). Simulating radiating and magnetized flows in multiple dimensions with ZEUS-MP. *The Astrophysical Journal - Supplement Series*, *165*(1), 188–228. https://doi.org/10.1086/504594

Huybrighs, H. L. F. (2023). Huybrighs et al., 2023 - simulations and documentation [Dataset]. Zenodo. https://doi.org/10.5281/ZENODO.8238510

Huybrighs, H. L. F., Roussos, E., Blöcker, A., Krupp, N., Futaana, Y., Barabash, S., et al. (2021). Reply to comment on "an active plume eruption on Europa during Galileo flyby E26 as indicated by energetic proton depletions". *Geophysical Research Letters*, *48*(18), e2021GL095240. https://doi.org/10.1029/2021GL095240

Huybrighs, H. L. F., Futaana, Y., Barabash, S., Wieser, M., Wurz, P., Krupp, N., et al. (2017). On the in-situ detectability of Europa's water vapour plumes from a flyby mission. *Icarus*, *289*, 270–280. https://doi.org/10.1016/j.icarus.2016.10.026

Huybrighs, H. L. F., Roussos, E., Blöcker, A., Krupp, N., Futaana, Y., Barabash, S., et al. (2020). An active plume eruption on Europa during Galileo flyby E26 as indicated by energetic proton depletions. *Geophysical Research Letters*, *47*(10), e2020GL087806. https://doi.org/10.1029/2020GL087806

Jaskulek, S. (1999). EPD SBAND MISSION Software Requirements, Revision K - Released Software, version 3, S1I-2-949-I (Technical report). https://doi.org/10.5281/zenodo.8238510

Jia, X., Kivelson, M. G., Khurana, K. K., & Kurth, W. S. (2018). Evidence of a plume on Europa from Galileo magnetic and plasma wave signatures. *Nature Astronomy*, *2*(6), 459–464. https://doi.org/10.1038/s41550-018-0450-z

Jia, X., Kivelson, M. G., & Paranicas, C. (2021). Comment on "an active plume eruption on Europa during Galileo flyby E26 as indicated by energetic proton depletions" by Huybrighs et al. *Geophysical Research Letters*, *48*(6), e2020GL091550. https://doi.org/10.1029/2020GL091550

Kivelson, M., Bagenal, F., Kurth, W., Neubauer, F. M., Paranicas, C., & Saur, J. (2004). Magnetospheric interactions with satellites. In F. Bagenal, T. E. Dowling, & W. McKinnon (Eds.), *Jupiter: The planet, satellites and magnetosphere*. Cambridge University Press.

Kivelson, M., Khurana, K., & Volwerk, M. (2009). Europa's interaction with the jovian magnetosphere. In R. T. Pappalardo, W. B. McKinnon, & K. Khurana (Eds.), *Europa* (pp. 545–570). University of Arizona Press.

Kollmann, P., Paranicas, C., Clark, G., Roussos, E., Lagg, A., & Krupp, N. (2016). The vertical thickness of Jupiter's Europa gas torus from charged particle measurements. *Geophysical Research Letters*, *43*(18), 9425–9433. https://doi.org/10.1002/2016gl070326

Kollmann, P., Paranicas, C., Lagg, A., Roussos, E., & Kusterer, M. (2022). Galileo/EPD user guide (Technical report). https://doi.org/10.1002/essoar.10503620.3

Kotova, A., Roussos, E., Krupp, N., & Dandouras, I. (2015). Modeling of the energetic ion observations in the vicinity of Rhea and Dione. *Icarus*, *258*, 402–417. https://doi.org/10.1016/j.icarus.2015.06.031

Kriegel, H., Simon, S., Motschmann, U., Saur, J., Neubauer, F. M., Persoon, A. M., et al. (2011). Influence of negatively charged plume grains on the structure of Enceladus' Alfvén wings: Hybrid simulations versus Cassini magnetometer data. *Journal of Geophysical Research*, *116*(A10). https://doi.org/10.1029/2011JA016842

Krupp, N., Kotova, A., Roussos, E., Simon, S., Liuzzo, L., Paranicas, C., et al. (2020). Magnetospheric interactions of Saturn's Moon Dione (2005–2015). *Journal of Geophysical Research: Space Physics*, *125*(6), e2019JA027688. https://doi.org/10.1029/2019JA027688

Lagg, A. (1998). *Energiereiche teilchen in der inneren jupitermagnetosphare: Simulation und ergebnisse des epd-experimentes an bord der raumsonde galileo (PhD thesis)*. Max Planck Institut Fur Aeronomie. Retrieved from http://meetings.mps.mpg.de/homes/lagg/downloads/lagg_thesis_1998.pdf

Lagg, A., Krupp, N., & Woch, J. (2003). In-situ observations of a neutral gas torus at Europa. *Geophysical Research Letters*, *30*(11), 1556. https://doi.org/10.1029/2003gl017214

Liuzzo, L., Paty, C., Cochrane, C., Nordheim, T., Luspay-Kuti, A., Castillo-Rogez, J., et al. (2021). Triton's variable interaction with Neptune's magnetospheric plasma. *Journal of Geophysical Research: Space Physics*, *126*(11), e2021JA029740. https://doi.org/10.1029/2021JA029740

Liuzzo, L., Poppe, A. R., Addison, P., Simon, S., Nénon, Q., & Paranicas, C. (2022). Energetic magnetospheric particle fluxes onto Callisto's atmosphere. *Journal of Geophysical Research: Space Physics*, *127*(11), e2022JA030915. https://doi.org/10.1029/2022JA030915

Liuzzo, L., Simon, S., & Regoli, L. (2019a). Energetic ion dynamics near Callisto. *Planetary and Space Science*, *166*, 23–53. https://doi.org/10.1016/j.pss.2018.07.014

Liuzzo, L., Simon, S., & Regoli, L. (2019b). Energetic electron dynamics near Callisto. *Planetary and Space Science*, *179*, 104726. https://doi.org/10.1016/j.pss.2019.104726

Mauk, B. H., Haggerty, D. K., Jaskulek, S. E., Schlemm, C. E., Brown, L. E., Cooper, S. A., et al. (2017). The Jupiter Energetic Particle Detector Instrument (JEDI) investigation for the juno mission. *Space Science Reviews*, *213*(1), 289–346. https://doi.org/10.1007/s11214-013-0025-3

McGrath, M. A., & Sparks, W. B. (2017). Galileo ionosphere profile coincident with repeat plume detection location at Europa. *Research Notes of the AAS*, *1*(1), 14. https://doi.org/10.3847/2515-5172/aa988e

Mitchell, D. G., Brandt, P. C., Roelof, E. C., Dandouras, J., Krimigis, S. M., & Mauk, B. H. (2005). Energetic neutral atom emissions from Titan interaction with Saturn's magnetosphere. *Science*, *308*(5724), 989–992. https://doi.org/10.1126/science.1109805

Modolo, R., & Chanteur, G. M. (2008). A global hybrid model for Titan's interaction with the Kronian plasma: Application to the Cassini Ta flyby. *Journal of Geophysical Research*, *113*(A1). https://doi.org/10.1029/2007JA012453

Nénon, Q., & André, N. (2019). Evidence of Europa neutral gas Torii from energetic sulfur ion measurements. *Geophysical Research Letters*, *46*(7), 3599–3606. https://doi.org/10.1029/2019GL082200

Nénon, Q., Sicard, A., Kollmann, P., Garrett, H. B., Sauer, S. P. A., & Paranicas, C. (2018). A physical model of the proton radiation belts of Jupiter inside Europa's orbit. *Journal of Geophysical Research: Space Physics*, *123*(5), 3512–3532. https://doi.org/10.1029/2018JA025216

Neubauer, F. (1980). Nonlinear standing Alfvén wave current system at Io: Theory. *Journal of Geophysical Research*, *85*(A3), 1171–1178. https://doi.org/10.1029/JA085iA03p01171

Neubauer, F. M. (1999). The sub-Alfvénic interaction of the Galilean satellites with the jovian magnetosphere. *Journal of Geophysical Research*, *103*(E9), 19843–19866. https://doi.org/10.1029/97JE03370

Nordheim, T. A., Regoli, L. H., Harris, C. D. K., Paranicas, C., Hand, K. P., & Jia, X. (2022). Magnetospheric ion bombardment of Europa's surface. *The Planetary Science Journal*, *3*(1), 5. https://doi.org/10.3847/psj/ac382a

Norman, M. L. (2000). Introducing ZEUS-MP: A 3D, parallel, multiphysics code for astrophysical fluid dynamics. *Revista Mexicana de Astronomia y Astrofisia Serie de Conferencias*, *9*(66–71).

Paganini, L., Villanueva, G. L., Roth, L., Mandell, A. M., Hurford, T. A., Retherford, K. D., & Mumma, M. J. (2019). A measurement of water vapour amid a largely quiescent environment on Europa. *Nature Astronomy*, *4*(3), 266–272. https://doi.org/10.1038/s41550-019-0933-6

Paranicas, C., Mauk, B. H., Khurana, K., Jun, I., Garrett, H., Krupp, N., & Roussos, E. (2007). Europa's near-surface radiation environment. *Geophysical Research Letters*, *34*(15). https://doi.org/10.1029/2007GL030834

Paranicas, C., McEntire, R. W., Cheng, A. F., Lagg, A., & Williams, D. J. (2000). Energetic charged particles near Europa. *Journal of Geophysical Research*, *105*(A7), 16005–16015. https://doi.org/10.1029/1999JA000350

Paranicas, C., Mitchell, D., Krimigis, S., Hamilton, D., Roussos, E., Krupp, N., et al. (2008). Sources and losses of energetic protons in Saturn's magnetosphere. *Icarus*, *197*(2), 519–525. https://doi.org/10.1016/j.icarus.2008.05.011

PDS. (2022). Galileo EPD data. https://doi.org/10.17189/n0dm-0014

Plainaki, C., Cassidy, T. A., Shematovich, V. I., Milillo, A., Wurz, P., Vorburger, A., et al. (2018). Towards a global unified model of Europa's tenuous atmosphere. *Space Science Reviews*, *214*(1), 40. https://doi.org/10.1007/s11214-018-0469-6

Plainaki, C., Massetti, S., Jia, X., Mura, A., Milillo, A., Grassi, D., et al. (2020). Kinetic simulations of the jovian energetic ion circulation around Ganymede. *The Astrophysical Journal*, *900*(1), 74. https://doi.org/10.3847/1538-4357/aba94c

Poppe, A. R., Fatemi, S., & Khurana, K. K. (2018). Thermal and energetic ion dynamics in Ganymede's magnetosphere. *Journal of Geophysical Research: Space Physics*, *123*(6), 4614–4637. https://doi.org/10.1029/2018JA025312

Regoli, L. H., Coates, A. J., Thomsen, M. F., Jones, G. H., Roussos, E., Waite, J. H., et al. (2016). Survey of pickup ion signatures in the vicinity of Titan using CAPS/IMS. *Journal of Geophysical Research: Space Physics*, *121*(9), 8317–8328. https://doi.org/10.1002/2016JA022617

Roth, L., Saur, J., Retherford, K. D., Strobel, D. F., Feldman, P. D., McGrath, M. A., & Nimmo, F. (2014). Transient water vapor at Europa's south pole. *Science*, *343*(6167), 171–174. https://doi.org/10.1126/science.1247051

Roussos, E., Cohen, C., Kollmann, P., Pinto, M., Krupp, N., Gonçalves, P., & Dialynas, K. (2022). A source of very energetic oxygen located in Jupiter's inner radiation belts. *Science Advances*, *8*(2), eabm4234. https://doi.org/10.1126/sciadv.abm4234

Roussos, E., Kollmann, P., Krupp, N., Paranicas, C., Krimigis, S., Mitchell, D., et al. (2012). Energetic electron observations of Rhea's magnetospheric interaction. *Icarus*, *221*(1), 116–134. https://doi.org/10.1016/j.icarus.2012.07.006

Schilling, N., Neubauer, F. M., & Saur, J. (2007). Time-varying interaction of Europa with the jovian magnetosphere: Constraints on the conductivity of Europa's subsurface ocean. *Icarus*, *192*(1), 41–55. https://doi.org/10.1016/j.icarus.2007.06.024

Selesnick, R. S., & Cohen, C. M. S. (2009). Charge states of energetic ions in Jupiter's radiation belt inferred from absorption microsignatures of Io. *Journal of Geophysical Research*, *114*(A1). https://doi.org/10.1029/2008JA013722

Shprits, Y. Y., Menietti, J. D., Drozdov, A. Y., Horne, R. B., Woodfield, E. E., Groene, J. B., et al. (2018). Strong whistler mode waves observed in the vicinity of Jupiter's moons. *Nature Communications*, *9*(1), 3131. https://doi.org/10.1038/s41467-018-05431-x

Snowden, D., & Higgins, A. (2021). A Monte Carlo model of energy deposition, ionization, and sputtering due to thermal ion precipitation into Titan's upper atmosphere. *Icarus*, *354*, 113929. https://doi.org/10.1016/j.icarus.2020.113929

Snowden, D., Smith, M., Jimson, T., & Higgins, A. (2018). Energy deposition and ion production from thermal oxygen ion precipitation during Cassini's T57 flyby. *Icarus*, *305*, 186–197. https://doi.org/10.1016/j.icarus.2018.01.014

Sparks, W. B., Hand, K. P., McGrath, M. A., Bergeron, E., Cracraft, M., & Deustua, S. E. (2016). Probing for evidence of plumes on Europa with HST/STIS. *The Astrophysical Journal*, *829*(2), 121. https://doi.org/10.3847/0004-637x/829/2/121

Sparks, W. B., Richter, M., de Witt, C., Montiel, E., Russo, N. D., Grunsfeld, J. M., et al. (2019). A search for water vapor plumes on Europa using SOFIA. *The Astrophysical Journal*, *871*(1), L5. https://doi.org/10.3847/2041-8213/aafb0a

Sparks, W. B., Schmidt, B. E., McGrath, M. A., Hand, K. P., Spencer, J. R., Cracraft, M., & Deustua, S. E. (2017). Active cryovolcanism on Europa? *The Astrophysical Journal*, *839*(2), L18. https://doi.org/10.3847/2041-8213/aa67f8

Tippens, T., Liuzzo, L., & Simon, S. (2022). Influence of Titan's variable electromagnetic environment on the global distribution of energetic neutral atoms. *Journal of Geophysical Research: Space Physics*, *127*(10), e2022JA030722. https://doi.org/10.1029/2022JA030722

Volwerk, M., Khurana, K., & Kivelson, M. (2007). Europa's Alfvén wing: Shrinkage and displacement influenced by an induced magnetic field. *Annales Geophysicae*, *25*(4), 905–914. https://doi.org/10.5194/angeo-25-905-2007

Williams, D. J., McEntire, R. W., Jaskulek, S., & Wilken, B. (1992). The Galileo energetic particles detector. *Space Science Reviews*, *60*(1), 385–412. https://doi.org/10.1007/BF00216863

Winterhalder, T. O., & Huybrighs, H. L. (2022). Assessing juice's ability of in situ plume detection in Europa's atmosphere. *Planetary and Space Science*, *210*, 105375. https://doi.org/10.1016/j.pss.2021.105375

Wulms, V., Saur, J., Strobel, D. F., Simon, S., & Mitchell, D. G. (2010). Energetic neutral atoms from Titan: Particle simulations in draped magnetic and electric fields. *Journal of Geophysical Research*, *115*(A6). https://doi.org/10.1029/2009JA014893